

Radiation from a dipole perpendicular to the interface between two planar semi-infinite magnetoelectric media

O. J. Franca*

*Institut für Physik, Universität Kassel, Heinrich-Plett-Straße 40, 34132 Kassel, Germany and
Instituto de Ciencias Nucleares,
Universidad Nacional Autónoma de México,
04510 México, Distrito Federal, México*

Luis F. Urrutia†

*Instituto de Ciencias Nucleares,
Universidad Nacional Autónoma de México,
04510 México, Distrito Federal, México
(Dated: July 15, 2021)*

We consider two semi-infinite magnetoelectric media with constant dielectric permittivity separated by a planar interface, whose electromagnetic response is described by non-dynamical axion electrodynamics and investigate the radiation of a point-like electric dipole located perpendicularly to the interface. We start from the exact Green's function for the electromagnetic potential, whose far-field approximation is obtained using a modified steepest descent approximation. This procedure yields the standard spherical waves as well as axially symmetric cylindrical superficial waves, which nevertheless are restricted to a region very close to the interface. We compute the angular distribution of the radiation and the total radiated power finding different interference patterns, depending on the relative position dipole-observer, and polarization mixing effects which are all absent in the standard dipole radiation. They are a manifestation of the magnetoelectric effect induced by axion electrodynamics. We illustrate our findings with some numerical estimations employing realistic media as well as some hypothetical choices in order to illuminate the effects of the magnetoelectric coupling which is usually very small.

PACS numbers: 78.20.Ci, 41.20.Jb, 11.55.Fv

Keywords: Magnetoelectric effect; Dipole radiation; Electromagnetic wave propagation

* francamentesantiago@ciencias.unam.mx

† urrutia@nucleares.unam.mx

I. INTRODUCTION

The radiation produced by an electric dipole near a planar interface has been well studied over the years and has remained a relevant subject of research for physicists and engineers due its relevance in a wide range of phenomena like practical applications in radio communications [1], THz Zenneck wave propagation [2], near-field optics [3], plasmonics [4] and nanophotonics [5], just to mention a few examples. In 1909, Sommerfeld [6] published a theory for a radiating vertically oriented dipole above a planar and lossy ground using Hertzian potentials. He found two kind of solutions which were asymptotic: spherical waves and surface waves [7]. Sommerfeld's approach formed the basis for subsequent investigations which included the case of an horizontally oriented radiating dipole in 1911 [8, 9]. Later, in 1919, Weyl [10] expressed the problem as a superposition of plane and evanescent waves and similar approaches were developed by Strutt [11], and Van der Pol and Niessen [12]. Later, Agarwal used the Weyl representation to promote the theory to its quantum version [13]. Probably, by the fact that the early theory of dipole emission near planar interfaces was written in German, although there was an English version summarized in Sommerfeld's lectures on theoretical physics [14], many aspects of the theory were reinvented and clarified over the years [15–18].

The discovery of new materials with exceptional electromagnetic properties further motivates the reconsideration of the radiative phenomena in these media. Here we consider planar interfaces constructed with linear homogeneous and isotropic magnetoelectric (ME) media giving rise to the so called magnetoelectric effect (MEE), whereby electric (magnetic) fields are able to induce additional (polarization) magnetization (polarization) in the material. This effect, which was predicted [19] and discovered [20] in antiferromagnets, has been widely studied along the years in multiferroic materials and it is codified in an additional parameter of the material: the magnetoelectric polarizability (MEP) [21]. The recent discovery of three-dimensional topological insulators (TIs) has boosted the interest in this topic by providing new materials where this effect is predicted to occur [22–27]. Generally speaking, TIs belong to a novel state of matter protected by time-reversal-symmetry (TRS) which admit an insulating bulk together with conducting surface states [28, 29]. The imposition of this symmetry yields two classes of materials: standard insulators labeled by a zero MEP and TIs characterized by a MEP equal to π .

The effective theoretical framework to deal with magnetoelectric media starts from axion electrodynamics [30], which consists of adding the term $\mathcal{L}_\vartheta = -(\alpha/4\pi^2)\vartheta(t, \mathbf{x}) \mathbf{E} \cdot \mathbf{B}$ to the Maxwell Lagrangian density \mathcal{L}_{em} , where α is the fine structure constant, \mathbf{E} is the electric field and \mathbf{B} is the magnetic field. The so called axion field $\vartheta(t, \mathbf{x})$ was introduced in Ref. [31] to propose a solution for the strong CP problem in strong interactions [32, 33]. This dynamical field, which weakly interacts with the photon, has been long sought as a viable candidate for dark matter [34]. In our case we restrict ourselves to a non-dynamical axion field, to be called the magnetoelectric polarizability (MEP) and which we consider as an additional electromagnetic property of the medium, in the same footing as its permittivity and permeability [25, 35, 36]. We call ϑ -Electrodynamics (ϑ -ED) this restriction of axion electrodynamics and our purpose is to study the radiation produced by a dipole oriented vertically with respect to the interface between two semi-infinite planar magnetoelectric media, having different constant MEPs. Excluding important differences in their microscopic structure, we will refer to the medium as a magnetoelectric, or a ϑ -medium, as long as its macroscopic electromagnetic response can be described in the framework of the ϑ -ED.

The paper is organized as follows. In section II, we present a review of ϑ -ED which also contains a summary of the calculation of the time-dependent Green's function (GF) for the 4-potential A^μ in our setup. As the source of the electromagnetic fields, in section III we introduce an oscillating vertically oriented point-like electric dipole located at a distance $z_0 > 0$, on the z -axis perpendicular to the interface between the two media. The convolution of this source with the GF is carried out in the subsection III A and yields the corresponding electromagnetic potentials A^μ in terms of closed integrals which are calculated in the Appendix A. The next step is to obtain the far-field approximation of those integrals. This is performed using a modified version of the steepest descent method, which is appropriate to the situation where the integrand is not a smooth function in the vicinity of the stationary phase due to the appearance of poles in the steepest descent path at this point. This approximation is carefully carried out in the Appendix B and relies heavily upon Ref. [15]. As a consequence of the approximation method we find that the 4-potential has two contributions: spherical waves and axially symmetric cylindrical surface waves. A detailed analysis on the latter allows us to introduce what we call the discarding angle θ_0 , both in the upper hemisphere (UH) and in the lower hemisphere (LH), which permits us to divide the space in two regions: \mathcal{V}_1 where the surface wave contribution can be neglected and \mathcal{V}_2 where this contribution has to be considered. In subsection III B the far-field expressions for \mathbf{E} and \mathbf{B} are calculated for each region. The fields in the region \mathcal{V}_1 are analyzed in subsection III B 1 where we emphasize how the phase of the field in standard ED changes due to presence of the ϑ -media, thus explaining the origin of different radiation patterns depending on the relative position of the dipole and the observer with respect to the interface. On the other hand, in Subsection III B 2 we study the fields in the region \mathcal{V}_2 and we find that the electric field exhibits a contribution of an axially symmetric cylindrical surface wave arising from the contribution of the pole in the modified steepest descent method. In section IV we consider the angular distribution, the total radiated power and the energy transport of the dipolar radiation. In the subsection IV A we establish the numerical parameters to

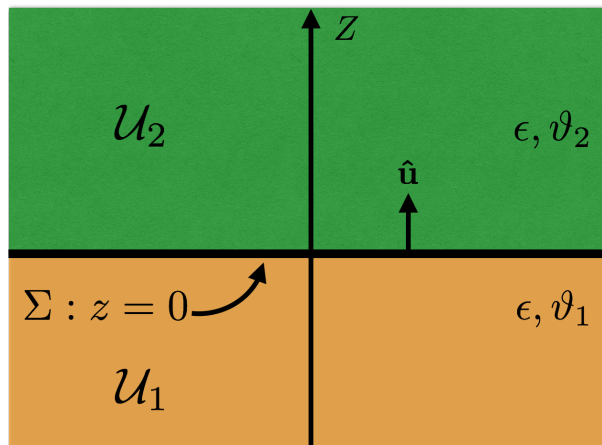


Figure 1: Two semi-infinite non-magnetic magnetoelectric media with different magnetoelectric polarizabilities ϑ_1 and ϑ_2 , having the same permittivity ϵ and separated by the planar interface Σ .

be used in the subsequent applications. Section IV B comprises a detailed examination of the angular distribution spectrum $dP/d\Omega$ in the region \mathcal{V}_1 . The behavior of this quantity separates naturally in two alternatives according to the following conditions: (i) the Case $(-)$, when the dipole and the observer are in different semi-spaces, and (ii) the Case $(+)$ otherwise. The resulting angular distributions for Case $(-)$ looks very similar to that of an electric dipole in electrodynamics, except for important modifications in its magnitude. However, the angular distribution for Case $(+)$ shows that new radiation patterns arise due to the MEE and which are further illustrated in two-dimensional polar plots. In section IV C, we calculate the power radiated into the region \mathcal{V}_1 for both Cases $(-)$ and $(+)$. Section IV D is devoted to the energy transport of the radiation in the region \mathcal{V}_2 . Here we also give some numerical estimations considering the media already discussed in Secs. IV B and IV C, plus some additional hypothetical choices. Let us insist again that our approach is based on the effective electromagnetic response of magnetoelectrics encoded in ϑ -ED. From this point of view we assume that any material we refer to has been fully characterized, meaning that their macroscopic parameters have been already determined. Finally, Sec. V provides a concluding summary and the conclusions from our results. In the Appendix A we derive the exact expressions for the potential A_μ required to calculate the electromagnetic fields, in terms of some basic integrals. The far-field approximation of those integrals is carried out in the Appendix B using a modified steepest descent method. The final Appendix C includes a brief review of the Faddeeva plasma dispersion function which arises in the discussion of the surface waves. Throughout this paper we use Gaussian units with $\hbar = c = 1$, the metric signature is $(+, -, -, -)$ and $\varepsilon^{0123} = 1$. We follow the conventions of Ref. [37].

II. ϑ -ELECTRODYNAMICS

Let us consider the situation where two semi-infinite ϑ -media are separated by a planar interface Σ located at $z = 0$, filling the regions \mathcal{U}_1 and \mathcal{U}_2 of the space, as shown in Fig. (1). We take both media to be non-magnetic, i.e. $\mu_1 = \mu_2 = 1$ and with the same permittivity $\epsilon_1 = \epsilon_2 = \epsilon$. This condition is motivated by the results in Ref. [38], which show that the effects of the MEE are substantially enhanced with respect to the optical contributions when both ϑ -media have the same dielectric constant and permeability. Also, in our case we want to eliminate the possibility of forbidden light zones related to the dipole's evanescent fields, which arise whenever a magnetic or electric dipole radiates in the presence of two media with different permittivities [39, 40]. These restrictions will help us to isolate the effects arising from changes in ϑ only. Additionally we assume the parameter ϑ to be piecewise constant so that it takes the values $\vartheta = \vartheta_1$ in the region \mathcal{U}_1 and $\vartheta = \vartheta_2$ in the region \mathcal{U}_2 . This is expressed as

$$\vartheta(\mathbf{x}) = \Theta(z)\vartheta_2 + \Theta(-z)\vartheta_1, \quad (1)$$

where $\Theta(z)$ is the standard Heaviside function with $\Theta(z) = 1$, $z \geq 0$ and $\Theta(z) = 0$, $z < 0$. The dynamics is governed by the standard Maxwell equations in a material medium [37, 41]

$$\nabla \cdot \mathbf{D} = 4\pi\rho, \quad \nabla \times \mathbf{H} = \frac{\partial \mathbf{D}}{\partial t} + 4\pi\mathbf{j}, \quad (2)$$

$$\nabla \cdot \mathbf{B} = 0, \quad \nabla \times \mathbf{E} = -\frac{\partial \mathbf{B}}{\partial t}, \quad (3)$$

with the constitutive relations

$$\mathbf{D} = \epsilon \mathbf{E} - \frac{\alpha}{\pi} \vartheta(z) \mathbf{B}, \quad \mathbf{H} = \mathbf{B} + \frac{\alpha}{\pi} \vartheta(z) \mathbf{E}. \quad (4)$$

Here α is the fine-structure constant, ϱ and \mathbf{j} are the external sources given by the charge and current densities respectively. The MEP given in Eq. (1) yields the following inhomogeneous equations

$$\epsilon \nabla \cdot \mathbf{E} = 4\pi \varrho + \tilde{\theta} \delta(z) \mathbf{B} \cdot \hat{\mathbf{u}}, \quad (5)$$

$$\nabla \times \mathbf{B} - \epsilon \frac{\partial \mathbf{E}}{\partial t} = 4\pi \mathbf{j} + \tilde{\theta} \delta(z) \mathbf{E} \times \hat{\mathbf{u}}. \quad (6)$$

where $\hat{\mathbf{u}}$ is the outward unit normal to the region \mathcal{U}_1 and

$$\tilde{\theta} = \alpha(\vartheta_2 - \vartheta_1)/\pi. \quad (7)$$

In the case of a TI located in the region \mathcal{U}_2 of Fig. 1 ($\vartheta_2 = \pi$) in front of a regular insulator ($\vartheta = 0$) in region \mathcal{U}_1 , we have

$$\tilde{\theta} = \alpha(2\tilde{m} + 1), \quad (8)$$

with \tilde{m} being an integer depending on the details of the TRS breaking at the interface between the two materials. We observe that Eqs. (5) and (6) can also be derived from the total Lagrangian density $\mathcal{L}_{\text{em}} + \mathcal{L}_\vartheta$ discussed in the Introduction. The homogeneous equations (3) still enable us to define the electromagnetic fields \mathbf{E} and \mathbf{B} in terms of the electromagnetic potentials Φ and \mathbf{A} as

$$\mathbf{E} = -\frac{\partial \mathbf{A}}{\partial t} - \nabla \Phi, \quad \mathbf{B} = \nabla \times \mathbf{A}, \quad A^\mu = (\Phi, \mathbf{A}). \quad (9)$$

The Eqs. (5) and (6) explicitly show that there are no modifications to the dynamics in the bulk ($z \neq 0$) with respect to standard ED. In this way, all the effects induced by \mathcal{L}_ϑ arise on the interface between the media ($z = 0$) and will manifest themselves as a consequence of the boundary conditions there. This is because the term $\mathbf{E} \cdot \mathbf{B}$ in the Lagrangian density is a total derivative, as can be readily verified from its expression in terms of the potential A^μ by recalling that $\mathbf{E} \cdot \mathbf{B} \sim \epsilon^{\alpha\beta\mu\nu} F_{\alpha\beta} F_{\mu\nu} \sim \partial_\alpha (\epsilon^{\alpha\beta\mu\nu} A_\beta F_{\mu\nu})$. In this way the modifications to the dynamics arise only when the integration by parts produces $\partial_\alpha \vartheta \neq 0$. Assuming that the time derivatives of the fields are finite in the vicinity of the surface Σ , the modified Maxwell equations (5) and (6) imply the following boundary conditions (BCs)

$$\epsilon [\mathbf{E}_z]_{z=0^-}^{z=0^+} = \tilde{\theta} \mathbf{B}_z|_{z=0}, \quad [\mathbf{B}_\parallel]_{z=0^-}^{z=0^+} = -\tilde{\theta} \mathbf{E}_\parallel|_{z=0}, \quad [\mathbf{B}_z]_{z=0^-}^{z=0^+} = 0, \quad [\mathbf{E}_\parallel]_{z=0^-}^{z=0^+} = 0, \quad (10)$$

for vanishing external sources on Σ . The notation is $[\mathbf{V}]_{z=0^-}^{z=0^+} = \mathbf{V}(z=0^+) - \mathbf{V}(z=0^-)$, $\mathbf{V}|_{z=0} = \mathbf{V}(z=0)$, where $z = 0^\pm$ indicates the limits $z = 0 \pm \eta$, with $\eta \rightarrow 0$, respectively. The first two equations in (10) require that their right-hand sides are well defined at the interface, which is guaranteed by the remaining boundary conditions. The continuous terms in the right-hand side of the first and second equations in (10) represent self-induced surface charge and surface current densities, respectively. These BCs clearly demonstrate the MEE, which is localized just at the interface between the two media.

A convenient way to deal with the fields produced by arbitrary sources in electrodynamics, in particular in ϑ -ED, is by using the corresponding Green function $G^\mu_\nu(x, x')$, which we briefly revise below [42–44]. In what follows we restrict ourselves to contributions of free sources $J^\mu = (\varrho, \mathbf{j})$ located outside the interface Σ , and to systems without BCs imposed on additional surfaces, except for those at infinity. A compact formulation of the problem is given in terms of the potentials (9) expressed in their four dimensional form $A^\mu = (\Phi, \mathbf{A})$, in terms of which the BCs (10) are

$$[A^\mu]_{z=0^-}^{z=0^+} = 0, \quad [\epsilon \partial_z A^0]_{z=0^-}^{z=0^+} = -\tilde{\theta} \epsilon^{30\alpha}{}_\nu \partial_\alpha A^\nu|_{z=0}, \quad [\partial_z A^i]_{z=0^-}^{z=0^+} = -\tilde{\theta} \epsilon^{3i\alpha}{}_\nu \partial_\alpha A^\nu|_{z=0}. \quad (11)$$

The Green function (GF) is such that

$$A^\mu(x) = \int d^4x' G^\mu_\nu(x, x') J^\nu(x'), \quad (12)$$

and satisfies the equation

$$[\diamond^\mu{}_\nu - \tilde{\theta} \delta(z) \epsilon^{3\mu\alpha}{}_\nu \partial_\alpha] G^\nu{}_\sigma(x, x') = 4\pi \eta^\mu{}_\sigma \delta(x - x'), \quad (13)$$

in the modified Lorenz gauge $\epsilon \partial \Phi / \partial t + \nabla \cdot \mathbf{A} = 0$, together with the BCs in Eqs. (11). The operator \diamond^μ_ν is

$$\diamond^\mu_\nu = (\epsilon \square^2, \square^2 \delta^i_j), \quad \square^2 = \epsilon \partial_t^2 - \nabla^2. \quad (14)$$

The detailed calculation of the GF is reported in Sec. III of Ref. [44]. Here we only recall the results that are written in terms of \bar{G}^μ_ν , which differs from G^μ_ν only in the term $G^0_0 = \bar{G}^0_0/\epsilon$. Since the GF is time-translational-invariant it is convenient to introduce the corresponding Fourier transform such that

$$\bar{G}^\mu_\nu(\mathbf{x}, \mathbf{x}', t - t') = \int_{-\infty}^{+\infty} \frac{d\omega}{2\pi} e^{-i\omega(t-t')} \bar{G}^\mu_\nu(\mathbf{x}, \mathbf{x}'; \omega). \quad (15)$$

The final result is presented as the sum of three terms, $\bar{G}^\mu_\nu(\mathbf{x}, \mathbf{x}'; \omega) = \bar{G}^\mu_{ED\ \nu}(\mathbf{x}, \mathbf{x}'; \omega) + \bar{G}^\mu_{\tilde{\theta}\ \nu}(\mathbf{x}, \mathbf{x}'; \omega) + \bar{G}^\mu_{\tilde{\theta}^2\ \nu}(\mathbf{x}, \mathbf{x}'; \omega)$, whose explicitly form is

$$\begin{aligned} \bar{G}^\mu_{ED\ \nu}(\mathbf{x}, \mathbf{x}'; \omega) &= \eta^\mu_\nu 4\pi \int \frac{d^2 \mathbf{k}_\perp}{(2\pi)^2} e^{i\mathbf{k}_\perp \cdot \mathbf{R}_\perp} \frac{ie^{i\sqrt{\tilde{k}_0^2 - \mathbf{k}_\perp^2}|z-z'|}}{2\sqrt{\tilde{k}_0^2 - \mathbf{k}_\perp^2}}, \\ \bar{G}^\mu_{\tilde{\theta}\ \nu}(\mathbf{x}, \mathbf{x}'; \omega) &= i\epsilon^\mu_\nu \alpha^3 \frac{4\pi\tilde{\theta}}{4n^2 + \tilde{\theta}^2} \int \frac{d^2 \mathbf{k}_\perp}{(2\pi)^2} e^{i\mathbf{k}_\perp \cdot \mathbf{R}_\perp} k_\alpha \frac{e^{i\sqrt{\tilde{k}_0^2 - \mathbf{k}_\perp^2}(|z|+|z'|)}}{\tilde{k}_0^2 - \mathbf{k}_\perp^2}, \\ \bar{G}^\mu_{\tilde{\theta}^2\ \nu}(\mathbf{x}, \mathbf{x}'; \omega) &= \frac{i4\pi\tilde{\theta}^2}{4n^2 + \tilde{\theta}^2} \int \frac{d^2 \mathbf{k}_\perp}{(2\pi)^2} [k^\mu k_\nu - (\eta^\mu_\nu + n^\mu n_\nu) k^2] e^{i\mathbf{k}_\perp \cdot \mathbf{R}_\perp} \frac{e^{i\sqrt{\tilde{k}_0^2 - \mathbf{k}_\perp^2}(|z|+|z'|)}}{2(\tilde{k}_0^2 - \mathbf{k}_\perp^2)^{3/2}}. \end{aligned} \quad (16)$$

Here $\mathbf{R}_\perp = (\mathbf{x} - \mathbf{x}')_\perp = (x - x', y - y')$ and $\mathbf{k}_\perp = (k_x, k_y)$ is the momentum parallel to the interface Σ , $k^\alpha = (\omega, \mathbf{k}_\perp)$ and $\tilde{k}_0 = n\omega$ where $n = \sqrt{\epsilon}$ is the refraction index. We observe that in the static limit ($\omega = 0$), the result (16) reduces to the one reported in Ref. [42]. The integral in $\bar{G}^\mu_{ED\ \nu}$ has been well studied in the literature and it gives the analytic result (A2) obtained by Sommerfeld [6, 9, 45] and Weyl [10].

III. ELECTRIC DIPOLE PERPENDICULAR TO THE INTERFACE Σ

In this section we determine the electric field of an oscillating point-like electric dipole $\mathbf{p} = p\hat{\mathbf{z}}$ located at a distance $z_0 > 0$ on the z -axis and perpendicular to the interface Σ (See Fig. 1). We restrict ourselves to the far-field approximation ($\tilde{k}_0 r \gg 1$) starting from the GFs given by Eqs. (16).

A. The Electromagnetic Potential A^μ

The charge and current density for this dipole are

$$\varrho(\mathbf{x}'; \omega) = -p\delta(x')\delta(y')\delta'(z' - z_0), \quad \mathbf{j}(\mathbf{x}'; \omega) = -i\omega p\delta(x')\delta(y')\delta(z' - z_0)\hat{\mathbf{z}}, \quad (17)$$

respectively, where $\delta'(u) = d\delta(u)/du$. After convoluting the sources (17) with the GFs (16) we find the following components of A^μ

$$A^0(\mathbf{x}; \omega) = -\frac{p}{n^2} i\tilde{k}_0 \cos\theta \frac{e^{i\tilde{k}_0(r-z_0 \cos\theta)}}{r} - \frac{1}{n^2} \frac{\tilde{\theta}^2 p}{4n^2 + \tilde{\theta}^2} \mathcal{H}(\mathbf{x}, z_0; \omega), \quad (18)$$

$$A^a(\mathbf{x}; \omega) = -\frac{2\tilde{\theta}p}{4n^2 + \tilde{\theta}^2} \frac{i\epsilon^{ab}x^b}{\rho} \frac{\partial}{\partial\rho} \mathcal{I}(\mathbf{x}, z_0; \omega) + \frac{\tilde{\theta}^2 p}{4n^2 + \tilde{\theta}^2} \frac{i\omega x^a}{\rho} \frac{\partial}{\partial\rho} \mathcal{J}(\mathbf{x}, z_0; \omega), \quad (19)$$

$$A^3(\mathbf{x}; \omega) = -i\omega p \frac{e^{i\tilde{k}_0(r-z_0 \cos\theta)}}{r}, \quad (20)$$

where $\rho = \|\mathbf{x}_\perp\| = \sqrt{x^2 + y^2}$, $r = \sqrt{x^2 + y^2 + z^2}$, $a, b \in \{1, 2\}$, $\varepsilon^{ab} = -\varepsilon^{ba}$, $\varepsilon^{12} = +1$, and $\{x^a\} = \{x^1, x^2\}$ with $x^1 = x$, $x^2 = y$. We also have the functions

$$\mathcal{H}(\mathbf{x}, z_0; \omega) = \int_0^\infty \frac{k_\perp^3 dk_\perp}{\tilde{k}_0^2 - k_\perp^2} J_0(k_\perp \rho) e^{i\sqrt{\tilde{k}_0^2 - k_\perp^2}(|z| + z_0)}, \quad (21)$$

$$\mathcal{I}(\mathbf{x}, z_0; \omega) = \int_0^\infty \frac{k_\perp dk_\perp}{\sqrt{\tilde{k}_0^2 - k_\perp^2}} J_0(k_\perp \rho) e^{i\sqrt{\tilde{k}_0^2 - k_\perp^2}(|z| + z_0)}, \quad (22)$$

$$\mathcal{J}(\mathbf{x}, z_0; \omega) = \int_0^\infty \frac{k_\perp dk_\perp}{\tilde{k}_0^2 - k_\perp^2} J_0(k_\perp \rho) e^{i\sqrt{\tilde{k}_0^2 - k_\perp^2}(|z| + z_0)}. \quad (23)$$

The derivation of the above results can be found in the Appendix A.

The next step is to calculate the integrals (21)-(23) in the far-field approximation. To this end we employ the steepest descent method [46–48] and incorporate some modifications based on the work of Refs. [15] and [49]. These modifications are required because the current integrals (21)-(23) have poles coinciding with their stationary point $(k_\perp)_s = \tilde{k}_0 \sin \theta$ at $\theta = \pi/2$, as can be seen in Eq. (B13) of the Appendix B. This means that the factor of the exponential is not a smooth function around the stationary point now, which will prevent a direct application of the method. The main idea to overcome this difficulty is to subtract and add the conflicting pole, as shown in Eqs. (B15) and (B27) of the Appendix B. Thereby, we obtain two integrals: one with the divergence removed in the vicinity of the stationary point and another containing the singularity, which can be directly evaluated. The first integral leads to the ordinary stationary phase contributions and the second one gives contributions that are identified as axially symmetric cylindrical surface waves [15]. The final results for the integrals \mathcal{H} , \mathcal{I} and \mathcal{J} , obtained in full detail in the Appendix B, are

$$\begin{aligned} \mathcal{H}(\mathbf{x}, z_0; \omega) = & \tilde{k}_0 \frac{e^{i\tilde{k}_0 r}}{ir} \left\{ \frac{\sin^2 \theta e^{i\tilde{k}_0 z_0 |\cos \theta|}}{|\cos \theta|} - \frac{1}{\sqrt{2(\sin \theta - \sin^2 \theta)}} \right\} \\ & + \sqrt{\frac{2}{\pi i \tilde{k}_0 r \sin \theta}} \frac{\tilde{k}_0^2}{i} e^{i\tilde{k}_0 r \sin \theta} \frac{\pi}{2} \operatorname{erfc} \left[-i\sqrt{i\tilde{k}_0 r (1 - \sin \theta)} \right], \end{aligned} \quad (24)$$

$$\begin{aligned} \mathcal{J}(\mathbf{x}, z_0; \omega) = & \frac{e^{i\tilde{k}_0 r}}{i\tilde{k}_0 r} \left\{ \frac{e^{i\tilde{k}_0 z_0 |\cos \theta|}}{|\cos \theta|} - \frac{1}{\sqrt{2(\sin \theta - \sin^2 \theta)}} \right\} \\ & + \sqrt{\frac{2}{\pi i \tilde{k}_0 r \sin \theta}} \frac{\pi e^{i\tilde{k}_0 r \sin \theta}}{2i} \operatorname{erfc} \left[-i\sqrt{i\tilde{k}_0 r (1 - \sin \theta)} \right], \end{aligned} \quad (25)$$

$$\mathcal{I}(\mathbf{x}, z_0; \omega) = \frac{e^{i\tilde{k}_0 r}}{ir} e^{i\tilde{k}_0 z_0 |\cos \theta|}, \quad (26)$$

where $\operatorname{erfc}(z)$ denotes the complementary error function defined in Eq. (C2). The contributions in curly brackets arise from the terms including the subtracted pole and they are well behaved at $\theta = 0, \pi/2, \pi$, as shown in Eqs. (B23) and (B24) for the function \mathcal{H} . A similar result follows for \mathcal{J} .

The contributions from the pole itself come through the erfc function, which modulates the amplitude of the surface waves behaving as $1/r^{1/2}$, and depends on the argument

$$i\sqrt{i}\sqrt{\tilde{k}_0 r (1 - \sin \theta)} = i\Lambda \equiv i\sqrt{i} s. \quad (27)$$

Recalling Eq. (C1), the complementary error function is proportional to $Z(e^{i\pi/4}s)$, where $Z(\Lambda)$ is the Faddeeva plasma dispersion function discussed in some detail in the Appendix C. In this way, the magnitude of the surface wave contribution is controlled by the function $F(s) = |Z(e^{i\pi/4}s)|^2/(2\pi)$ which can be readily calculated from Eq. (C10). This is a rapidly decreasing function with $F(0) = 0.5$, $F(1) \approx 0.112$ and $F(3) \approx 0.0174$. This behavior provides us with a way to assess the relevance of the surface waves. Let us consider $\tilde{k}_0 r$ large enough to describe the far-field regime. When $s \rightarrow \infty$ the function $F(s)$ tends to zero and the surface wave contribution can be neglected, whereas when $s \rightarrow 0$ the function $F(s)$ contributes maximally and the surface waves should be considered. If we recall that $\rho = r \sin \theta$, s^2 can be rewritten as $s^2 = \tilde{k}_0(r - \rho)$ and can be interpreted as a measure of how far the observer with coordinates (r, θ, ϕ) is from the interface Σ . In another words, s^2 determines how far is the spherical radius r from the cylindrical radius ρ at the observation point. This property enables us to define what we call the discarding angle θ_0 ,

which provides us with a condition to estimate when we can neglect or not the surface wave contribution, according to the magnitude of $F(s)$. For a given observation distance r we take the arbitrary cutoff point to be at $s = 1$, where the value of $F(s)$ has decreased about five times with respect to its maximum at $s = 0$ and define $\sin \theta_0 = 1 - 1/(\tilde{k}_0 r)$. More precisely, we can distinguish the UH $\theta \in [0, \pi/2]$ from the LH $\theta \in [\pi/2, \pi]$ by writing

$$\theta_0^{UH} = \arcsin\left(1 - \frac{1}{\tilde{k}_0 r}\right), \quad \theta_0^{LH} = \frac{\pi}{2} + \arccos\left(1 - \frac{1}{\tilde{k}_0 r}\right), \quad (28)$$

respectively. Let us observe that both discarding angles are very close to the interface ($\theta = \pi/2$) in the far-field regime.

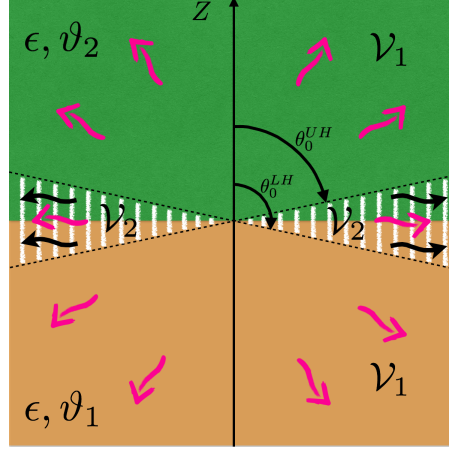


Figure 2: Diagram showing the regions \mathcal{V}_1 and \mathcal{V}_2 determined through the discarding angles θ_0^{UH} and θ_0^{LH} . The region \mathcal{V}_1 , where only the spherical waves (undulated pink arrows) are taken into account is defined by $\theta \in [0, \theta_0^{UH}] \cup (\theta_0^{LH}, \pi]$. The region \mathcal{V}_2 (white hatched region), defined by $\theta \in [\theta_0^{UH}, \theta_0^{LH}]$, is where both surface waves (undulated black waves) and spherical waves have to be taken into account.

The discarding angles define two regions, as shown in Fig. 2. The region \mathcal{V}_1 , where $\theta \in [0, \theta_0^{UH}] \cup (\theta_0^{LH}, \pi]$, is such that we can neglect the surface waves because $s > 1$, while in its complement, the region \mathcal{V}_2 where $\theta \in [\theta_0^{UH}, \theta_0^{LH}]$, we have to take into account the surface waves besides the standard $1/r$ contribution, since $s < 1$.

From the function $\text{erfc}\left(-i\sqrt{\tilde{k}_0 r(1 - \sin \theta)}\right)$ appearing in the Eqs. (24) and (25) we identify the analogous of the Sommerfeld numerical distance S in the standard dipole radiation, which is determined by rewriting the complementary error function as $\text{erfc}(-i\sqrt{S})$ [15]. Thus we have

$$S = i\tilde{k}_0 r(1 - \sin \theta) = is^2, \quad (29)$$

which varies with the angle θ for a fixed observation distance r . This quantity is closely related to the discarding angle θ_0 according to

$$|S| = \frac{1 - \sin \theta}{1 - \sin \theta_0}. \quad (30)$$

Going back to the calculation of the electromagnetic field in the far-field approximation, we now write the corresponding expressions for the electromagnetic potentials obtained from plugging the results (24-26) into the equations (18-20). In the case of the region \mathcal{V}_1 , where we neglect the surface waves, we have

$$A^0(\mathbf{x}; \omega) = -\frac{p}{n^2} i\tilde{k}_0 \cos \theta \frac{e^{i\tilde{k}_0(r - z_0 \cos \theta)}}{r} - \frac{1}{n^2} \frac{\tilde{\theta}^2 p}{4n^2 + \tilde{\theta}^2} \tilde{k}_0 \frac{\sin^2 \theta}{|\cos \theta|} \frac{e^{i\tilde{k}_0(r + z_0 |\cos \theta|)}}{ir}, \quad (31)$$

$$A^a(\mathbf{x}; \omega) = \frac{p}{4n^2 + \tilde{\theta}^2} \left[-2\tilde{\theta} i\tilde{k}_0 \left(\frac{\varepsilon^{ab} x^b}{r} \right) + \tilde{\theta}^2 \frac{i\omega}{|\cos \theta|} \left(\frac{x^a}{r} \right) \right] \frac{e^{i\tilde{k}_0(r + z_0 |\cos \theta|)}}{r}, \quad (32)$$

$$A^3(\mathbf{x}; \omega) = -i\omega p \frac{e^{i\tilde{k}_0(r - z_0 \cos \theta)}}{r}, \quad (33)$$

where we have dropped terms of $\mathcal{O}(r^{-2})$ and higher.

On the other hand, in the region \mathcal{V}_2 the contribution of the surface waves near the interface is apparent. The electromagnetic potential now is

$$A^0(\mathbf{x}; \omega) = \mp \frac{p}{n^2} i\tilde{k}_0 \xi \frac{e^{i\tilde{k}_0(r \mp z_0 \xi)}}{r} - \frac{1}{n^2} \frac{\tilde{\theta}^2 p}{4n^2 + \tilde{\theta}^2} \tilde{k}_0 \frac{e^{i\tilde{k}_0 r}}{ir} \left(i\tilde{k}_0 z_0 - \frac{\xi}{8} \right) - \frac{1}{n^2} \frac{\tilde{\theta}^2 p}{4n^2 + \tilde{\theta}^2} \tilde{k}_0^2 \sqrt{\frac{2}{\pi i \tilde{k}_0 r}} e^{i\tilde{k}_0 r} \left(\frac{\pi}{2i} + \sqrt{\frac{\pi i \tilde{k}_0 r}{2}} \xi \right), \quad (34)$$

$$A^a(\mathbf{x}; \omega) = \frac{p}{4n^2 + \tilde{\theta}^2} \left[-2i\tilde{\theta} \tilde{k}_0 \frac{\varepsilon^{ab} x^b}{\rho} \frac{e^{i\tilde{k}_0(r+z_0 \xi)}}{r} + \tilde{\theta}^2 i\omega \frac{x^a}{\rho} \frac{e^{i\tilde{k}_0 r}}{r} \left(i\tilde{k}_0 z_0 - \frac{\xi}{8} \right) - \tilde{\theta}^2 \omega \tilde{k}_0 \frac{x^a}{\rho} \sqrt{\frac{2}{\pi i \tilde{k}_0 r}} e^{i\tilde{k}_0 r} \left(\frac{\pi}{2i} + \sqrt{\frac{\pi i \tilde{k}_0 r}{2}} \xi \right) \right], \quad (35)$$

$$A^3(\mathbf{x}; \omega) = -i\omega p \frac{e^{i\tilde{k}_0(r \mp z_0 \xi)}}{r}, \quad (36)$$

after dropping terms of $\mathcal{O}(r^{-2})$ and higher. The minus (plus) sign in the first term of the right-hand side in Eq. (34) corresponds to the UH (LH), respectively. We have also performed a first order power expansion around $\pi/2$ in the complementary error function arising from Eqs. (24) and (25) in terms of the variable $\xi < 1$ given by

$$\xi^{UH} \equiv \pi/2 - \theta^{UH}, \quad \xi^{LH} = \theta^{LH} + \pi/2, \quad (37)$$

for the upper and lower hemispheres, respectively. Let us observe that for both hemispheres we have $\xi > 0$ and also that $(1 - \sin \theta) = \xi^2/2$. In analogous way it is convenient to introduce the corresponding variable ξ_0 related to the discarding angle θ_0 just by replacing $\xi \rightarrow \xi_0$ and $\theta \rightarrow \theta_0$ in Eq. (37). Using also Eq. (28) we obtain $\xi_0 = \sqrt{2/(n\omega r)}$. In this way $|S| = \xi^2/\xi_0^2 < 1$ for the upper and lower hemispheres. The expansion in powers of ξ is only valid when $\xi \ll \xi_0$.

B. The Electric Field

Since Faraday law (3) yields $\mathbf{B} = \sqrt{\epsilon} \hat{\mathbf{n}} \times \mathbf{E}$ in the far-field approximation we need to calculate only the electric field $\mathbf{E}(\mathbf{x}; \omega)$ to get a complete description of the radiation regime, where $\hat{\mathbf{n}} \cdot \mathbf{B} = 0$ is satisfied. The components of the electric field are calculated through

$$\mathbf{E}(\mathbf{x}; \omega) = -i\tilde{k}_0 \hat{\mathbf{n}} A^0(\mathbf{x}; \omega) + i\omega \mathbf{A}(\mathbf{x}; \omega). \quad (38)$$

1. The region \mathcal{V}_1

Substituting in Eq. (38) the previous expressions for $A^\mu(\mathbf{x}; \omega)$ in the region \mathcal{V}_1 we obtain the following electric field:

$$E^a(\mathbf{x}; \omega) = \left[-f_{\parallel}(\theta, z_0, \omega) \frac{zx^a}{r^2} + \frac{2\tilde{\theta}n}{4n^2 + \tilde{\theta}^2} e^{i\tilde{k}_0 z_0 |\cos \theta|} \frac{\varepsilon^{ab} x^b}{r} \right] \omega^2 p \frac{e^{i\tilde{k}_0 r}}{r},$$

$$E^3(\mathbf{x}; \omega) = \left[\sin^2 \theta f_{\parallel}(\theta, z_0, \omega) \right] \omega^2 p \frac{e^{i\tilde{k}_0 r}}{r}, \quad (39)$$

with

$$f_{\parallel}(\theta, z_0, \omega) = e^{-i\tilde{k}_0 z_0 \cos \theta} + \text{sgn}(\cos \theta) \frac{\tilde{\theta}^2}{4n^2 + \tilde{\theta}^2} e^{i\tilde{k}_0 z_0 |\cos \theta|}. \quad (40)$$

Here sgn denotes the sign function with the additional condition $\text{sgn}(0) = 0$. It is possible to verify that $\hat{\mathbf{n}} \cdot \mathbf{E} = 0$ as required for the electric field in the far-zone regime. The $x-y$ components of E^a in Eq. (39) which are not included in the f_{\parallel} term have their origin in the MEE which introduces a mixing reflection coefficient $R_{TE, TM}$ at the interface Σ , as we will explain later.

The main feature in the components of the electric field (39) is the presence of two different phases in the exponential related to the source variables $\mathbf{x}' = z_0 \hat{\mathbf{z}}$, which are specified by $\cos \theta$ and $|\cos \theta|$ as shown in Eq. (40). The first exponential contributes with the term $\exp \left[i \tilde{k}_0 (r - z_0 \cos \theta) \right]$ having the characteristic phase of dipole radiation in standard electrodynamics [37, 41]. On the other hand, the contributions arising from the new terms involving the MEP, which are proportional to $\tilde{\theta}$ and $\tilde{\theta}^2$, yield the exponential $\exp \left[i \tilde{k}_0 (r + z_0 |\cos \theta|) \right]$. As we will show in the next subsection, the modifications in the power spectrum of the dipolar radiation in our setting arise precisely due to the contribution $z_0 |\cos \theta|$ in the phase of the electric field. The dependence on the sign of $\cos \theta$ enforces two cases, which we denote as Case (−) and Case (+). The former case occurs when $|\cos \theta| = -\cos \theta$, i.e. when $\theta \in (\theta_0^{LH}, \pi]$ is in the LH. In this situation the three components of the electric field will have the same phase and we do not expect significant changes with respect to the usual angular dependence of the dipolar radiation because the phase of the electric field is that of standard electrodynamics. By contrast, the Case (+) takes place when $|\cos \theta| = \cos \theta$, which is realized for $\theta \in [0, \theta_0^{UH})$ in the UH. In this case the electric field presents two different phases which will interfere yielding new effects different from those in the usual dipolar radiation.

Finally, we analyze the function $f_{\parallel}(\theta, z_0, \omega)$ given by Eq. (40), which codifies the different phases of the electric field (39). For the Case (+), f_{\parallel} takes the following form

$$f_{\parallel}^+(\theta, z_0, \omega) = f_{\parallel}(\theta, z_0, \omega)|_{UH} = e^{-i \tilde{k}_0 z_0 \cos \theta} + \frac{\tilde{\theta}^2}{4n^2 + \tilde{\theta}^2} e^{i \tilde{k}_0 z_0 \cos \theta}. \quad (41)$$

On the other hand, for the Case (−), the function f_{\parallel} is

$$f_{\parallel}^-(\theta, z_0, \omega) = f_{\parallel}(\theta, z_0, \omega)|_{LH} = \frac{4n^2}{4n^2 + \tilde{\theta}^2} e^{-i \tilde{k}_0 z_0 \cos \theta}. \quad (42)$$

The functions f_{\parallel}^+ (f_{\parallel}^-) are comparable to $\Phi_1^{(1)}$ ($\Phi_2^{(1)}$) used in Ref. [40] to characterize the reflected (transmitted) electric dipole radiation that passes through the interface between two planar slabs with different dielectric constants. Motivated by this similarity, in the following we show that the factors $\tilde{\theta}^2/(4n^2 + \tilde{\theta}^2)$, $4n^2/(4n^2 + \tilde{\theta}^2)$ and $2\tilde{\theta}/(4n^2 + \tilde{\theta}^2)$ correspond to some reflection and transmission coefficients at the interface. This provides us with a nice opportunity to make contact with other results in the literature together with some alternative methods of calculation. The appearance of reflection and transmission coefficients at the interface Σ ($z = 0$) in the expressions for the fields in the region $\tilde{k}_0 r \rightarrow \infty$ is not quite immediate in our formulation. Its physical origin can be traced back to the method for calculating the fields employed in some references, like [40, 46], for example. In these cases the electric field in each region is built as a superposition of the field generated by the electric dipole (a parallel (TM) field for a vertically oriented electric dipole) plus an additional reflected or transmitted field satisfying the homogeneous Helmholtz equation. The imposition of the BCs at the interface Σ naturally introduces the corresponding reflection and transmitted coefficients (the Fresnel coefficients) which are subsequently inherited in the far-field approximation determining the radiation zone.

To validate the above statements in our case, let us start with the radiation fields in the UH by considering the general expression for the reflected electric field discussed in the Appendix B of Ref. [50], where the authors calculate the Green's function of a planar interface separating two semi-infinite TIs. The reflective part of the GF is written as

$$G^{ij}(\mathbf{x}, \mathbf{x}'; \omega) = \int \frac{d^2 \mathbf{k}_{\perp}}{(2\pi)^2} e^{i \mathbf{k}_{\perp} \cdot \mathbf{R}_{\perp}} \mathcal{R}^{ij}(\mathbf{k}_{\perp}, k_z, z, z'), \quad (43)$$

which connects the electric field components E^i directly with the current density j^k through the equation

$$E^i(\mathbf{x}; \omega) = -4\pi i \omega \int d^3 \mathbf{x}' G^{ik}(\mathbf{x}, \mathbf{x}'; \omega) j^k(\mathbf{x}'; \omega). \quad (44)$$

In our case only $j^3 = -i\omega p \delta(x') \delta(y') \delta(z' - z_0)$ is different from zero so that the only contributions to \mathcal{R}^{ij} come from \mathcal{R}^{i3} , which can be read from Eqs. (B8), (B10) and (B12) of Ref. [50] for an incident TM polarized plane wave, and which we rewrite here

$$\mathcal{R}^{13}(\mathbf{k}_{\perp}, k_z, z, z_0) = \frac{ie^{ik_z(z+z_0)}}{2k_z} \left[-\frac{k_x k_z}{k^2} R_{TM, TM} + \frac{k_y}{k} R_{TE, TM} \right], \quad (45)$$

$$\mathcal{R}^{23}(\mathbf{k}_{\perp}, k_z, z, z_0) = \frac{ie^{ik_z(z+z_0)}}{2k_z} \left[-\frac{k_y k_z}{k^2} R_{TM, TM} - \frac{k_x}{k} R_{TE, TM} \right], \quad (46)$$

$$\mathcal{R}^{33}(\mathbf{k}_{\perp}, k_z, z, z_0) = \frac{ie^{ik_z(z+z_0)}}{2k_z} \left[\frac{k_{\perp}^2}{k^2} R_{TM, TM} \right]. \quad (47)$$

Incidentally, the above equations show that the TM and TE polarizations are mixed as a consequence of the MEE. The explicit expressions for the reflection coefficients are given in Eqs. (44)-(46) of Ref. [50]. The notation in Ref. [50] $\{k, k_p, k_z\}$ is equivalent to ours $\{\tilde{k}_0, |\mathbf{k}_\perp|, \sqrt{\tilde{k}_0^2 - \mathbf{k}_\perp^2}\}$, respectively. In this way, the components of the electric field are

$$E^1(\mathbf{x}; \omega) = -4\pi i \omega^2 p \int \frac{d^2 \mathbf{k}_\perp}{(2\pi)^2} \frac{e^{ik_z z_0}}{2k_z} \left[-\frac{k_x k_z}{k^2} R_{TM, TM} + \frac{k_y}{k} R_{TE, TM} \right] e^{i\mathbf{k}_\perp \cdot \mathbf{R}_\perp} e^{ik_z z}, \quad (48)$$

$$E^2(\mathbf{x}; \omega) = -4\pi i \omega^2 p \int \frac{d^2 \mathbf{k}_\perp}{(2\pi)^2} \frac{e^{ik_z z_0}}{2k_z} \left[-\frac{k_y k_z}{k^2} R_{TM, TM} - \frac{k_x}{k} R_{TE, TM} \right] e^{i\mathbf{k}_\perp \cdot \mathbf{R}_\perp} e^{ik_z z}, \quad (49)$$

$$E^3(\mathbf{x}; \omega) = -4\pi i \omega^2 p \int \frac{d^2 \mathbf{k}_\perp}{(2\pi)^2} \frac{e^{ik_z z_0}}{2k_z} \left[\frac{k_\perp^2}{k^2} R_{TM, TM} \right] e^{i\mathbf{k}_\perp \cdot \mathbf{R}_\perp} e^{ik_z z}. \quad (50)$$

To compute the far-field approximation of the electric field written above, which is necessary to compare with our expressions (39) and (40), we make use of the angular spectrum representation method which we briefly review [40]. For fields satisfying the Helmholtz equation $(\nabla^2 + \kappa^2)\mathbf{E} = 0$, with $\kappa = \epsilon\omega$, which can be written as

$$E^i(x, y, z) = \int d^2 \mathbf{k}_\perp \hat{E}^i(k_x, k_y, z) e^{i\mathbf{k}_\perp \cdot \mathbf{x}_\perp}, \quad (51)$$

one can show that

$$\hat{E}^i(k_x, k_y, z) = \hat{E}^i(k_x, k_y, z=0) e^{\pm i k_z z}, \quad k_z = \sqrt{\kappa^2 - \mathbf{k}_\perp^2}, \quad \text{Im}(k_z) \geq 0, \quad (52)$$

choosing the $+$, $-$ signs according to $z > 0$ or $z < 0$, respectively. Substituting Eq. (52) into Eq.(51) yields the so-called angular spectrum representation of the electric field. One of the notable consequences of this approach is that the far-field approximation or the electric field is given in terms of the function $\hat{\mathbf{E}}(k_x, k_y, z=0)$. According to Ref.[40] we have

$$\begin{aligned} \mathbf{E}_{\tilde{k}_0 r \rightarrow \infty} \left(\frac{x}{r}, \frac{y}{r}, \frac{z}{r} \right) &= -2\pi i \tilde{k}_0 s_z \hat{\mathbf{E}}(k_x = \tilde{k}_0 s_x, k_y = \tilde{k}_0 s_y, z=0) \frac{e^{i\tilde{k}_0 r}}{r}, \\ s_x &= \sin \theta \cos \varphi, \quad s_y = \sin \theta \sin \varphi, \quad s_z = \cos \theta, \quad k_z = \tilde{k}_0 s_z = \tilde{k}_0 \cos \theta. \end{aligned} \quad (53)$$

Our next step is to identify the respective functions $\hat{E}^i(k_x, k_y, z=0)$ in each of the components (48)-(50), so that we can apply the relation (53). Making the required substitutions we find that

$$\hat{E}^i(k_x, k_y, z=0) = -i \frac{\omega^2 p}{2\pi k_z} e^{ik_z z_0} \left[\quad \right]^i, \quad (54)$$

where each square bracket $[\quad]^i$ denotes the corresponding one in Eqs. (48)-(50). Substituting in (53) yields

$$E_{\tilde{k}_0 r \rightarrow \infty}^1(\Omega) = \left[\frac{xz}{r^2} R_{TM, TM} - \frac{y}{r} R_{TE, TM} \right] p \omega^2 \frac{e^{i\tilde{k}_0 r}}{r} e^{i\tilde{k}_0 \cos \theta z_0}, \quad (55)$$

$$E_{\tilde{k}_0 r \rightarrow \infty}^2(\Omega) = \left[\frac{yz}{r^2} R_{TM, TM} + \frac{x}{r} R_{TE, TM} \right] p \omega^2 \frac{e^{i\tilde{k}_0 r}}{r} e^{i\tilde{k}_0 \cos \theta z_0}, \quad (56)$$

$$E_{\tilde{k}_0 r \rightarrow \infty}^3(\Omega) = \left[-\frac{|\mathbf{x}_\perp|^2}{r^2} R_{TM, TM} \right] p \omega^2 \frac{e^{i\tilde{k}_0 r}}{r} e^{i\tilde{k}_0 \cos \theta z_0}, \quad \frac{|\mathbf{x}_\perp|^2}{r^2} = \sin^2 \theta. \quad (57)$$

Comparing the above results with our expressions (39) and (40) for f_\parallel^+ yields the identifications

$$R_{TM, TM} = \frac{\tilde{\theta}^2}{4n^2 + \tilde{\theta}^2} \quad R_{TE, TM} = -\frac{2\tilde{\theta}n}{4n^2 + \tilde{\theta}^2}. \quad (58)$$

Carrying the analogous calculation for the LH with f_\parallel^- , we read the transmission coefficient

$$T_{TM, TM} = \frac{4n^2}{4n^2 + \tilde{\theta}^2}, \quad T_{TE, TM} = R_{TE, TM}. \quad (59)$$

We immediately verify that $R_{TM, TM} + T_{TM, TM} = 1$ as expected. Let us observe that the expressions for the transmission and reflection coefficients obtained from our calculation can be verified from the general expressions (43)-(46) in Ref. [50], after the following restrictions are made: $\epsilon_1 = \epsilon_2 = \epsilon = n^2$, $\mu_1 = \mu_2 = 1$, $k_{z1} = k_{z2} = k_z$ and $\Delta = \tilde{\theta}$.

2. The region \mathcal{V}_2

This region corresponds to what is normally called the intermediate region in the literature [15] and is characterized by the condition that the Sommerfeld numerical distance satisfies $S < 1$, in spite $\tilde{k}_0 r$ being large. Clearly this is possible because we are in the limit $\theta \rightarrow \pi/2$, ($\xi \rightarrow 0$), i.e. very close to the interface Σ .

The electric field is

$$\begin{aligned} E^a(\mathbf{x}; \omega) &= \left[\mp \xi \frac{x^a}{\rho} e^{\mp i \tilde{k}_0 z_0 \xi} + \frac{2 \tilde{\theta} n}{4n^2 + \tilde{\theta}^2} \frac{\varepsilon^{ab} x^b}{\rho} e^{i \tilde{k}_0 z_0 \xi} \right] p \omega^2 \frac{e^{i \tilde{k}_0 r}}{r}, \\ E^3(\mathbf{x}; \omega) &= \left[\frac{e^{\mp i \tilde{k}_0 z_0 \xi}}{r} \pm \frac{\tilde{\theta}^2}{4n^2 + \tilde{\theta}^2} \tilde{k}_0 \xi \left(\frac{i z_0}{r} + \frac{\pi}{2} \sqrt{\frac{2}{\pi i \tilde{k}_0 r}} \right) \right] p \omega^2 e^{i \tilde{k}_0 r}, \end{aligned} \quad (60)$$

where we have dropped terms $\mathcal{O}(\xi^2)$. The variable ξ was previously defined in Eq. (37) for each hemisphere. Also we verified that $\hat{\mathbf{n}} \cdot \mathbf{E} = 0$ using the approximations $\sin \theta \approx 1$ and $\cos \theta \approx \xi$, which are adequate for the region \mathcal{V}_2 . From Eq. (60) we observe the presence of surface waves, codified in the term proportional to $e^{i \tilde{k}_0 r} / \sqrt{r}$ [6]. They are also present in the standard case of dipolar radiation when two different electromagnetic media are separated by a planar interface. Nevertheless, in our case they only contribute when at least one of the media is magnetoelectric, i. e. when $\tilde{\theta} \neq 0$ defines the interface. This is because we have chosen two non-magnetic media with the same permittivity ϵ , which means that setting $\tilde{\theta} = 0$ yields an infinite media with no interface at all. An authoritative discussion of surface waves in dipolar radiation, including an historical perspective, is given in Ref. [15].

IV. ANGULAR DISTRIBUTION, TOTAL RADIATED POWER AND ENERGY TRANSPORT

A. The parameters

With the purpose of illustrating our results with some numerical estimations we need to fix the parameters defining our setup. Our choice is motivated by the fact that current magnetoelectric media are of great interest in atomic physics and optics, therefore we focus on the possibility that our results could be tested in the laboratory. In this way, we think as a dipolar source an atom with a given dipolar moment p , whose emission spectrum goes from the near infrared to the near ultraviolet. Furthermore, the magnetoelectric coupling is usually very small (of the order of the fine structure constant for TIs), so that appreciable effects will appear near the interface. In this way we have chosen the distance between the dipole and the observer to be lesser than 1 mm. For all cases in the following numerical estimations, with the exception of Fig. 6, we take the frequency $\omega = 1.5 \text{ eV}$ (362.7 THz or $\lambda = 826.6 \text{ nm}$) in the near infrared, the observer distance $r = 667 \text{ eV}^{-1}$ (0.131 mm), and the dipole location at $z_0 = 25 \text{ eV}^{-1}$ (4.94 μm). The far-field condition is well satisfied with $n \omega r \approx 1000 n$. The remaining free parameters are $\tilde{\theta}$ and n , which characterize the medium.

B. Angular distribution for the radiation in the region \mathcal{V}_1

In this subsection we obtain the angular distribution of radiated power associated to the electric field given by Eqs. (39) for the region \mathcal{V}_1 . Recalling that the electromagnetic fields satisfy $\hat{\mathbf{n}} \cdot \mathbf{E} = 0$ and $\mathbf{B} = \sqrt{\epsilon} \hat{\mathbf{n}} \times \mathbf{E}$ we obtain the standard Poynting vector in a material media with $\mu = 1$,

$$\mathbf{S} = \frac{1}{4\pi} \mathbf{E} \times \mathbf{H} = \frac{\sqrt{\epsilon}}{4\pi} \|\mathbf{E}\|^2 \hat{\mathbf{n}}, \quad (61)$$

where $\hat{\mathbf{n}}$ coincides with the direction of the phase velocity of the outgoing wave. According to Refs. [37, 41], the time-averaged power radiated per unit solid angle solid by a localized source is

$$\frac{dP}{d\Omega} = \frac{r^2}{2} \text{Re} \left[\frac{\mathbf{E}(\mathbf{x}; \omega) \times \mathbf{H}^*(\mathbf{x}; \omega)}{4\pi} \right] = \frac{n r^2}{8\pi} \mathbf{E}(\mathbf{x}; \omega) \cdot \mathbf{E}^*(\mathbf{x}; \omega). \quad (62)$$

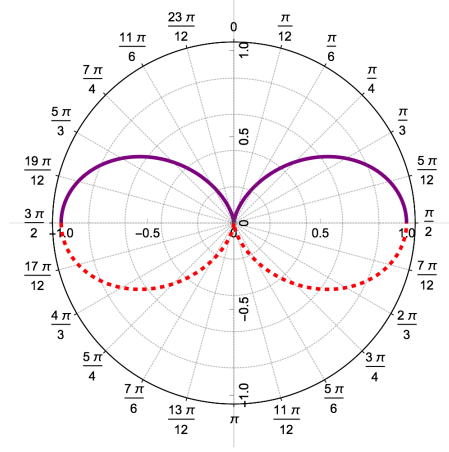


Figure 3: The SED case: polar plot of the angular distribution $dP/d\Omega$ for the radiated power produced by a dipole in an infinite non-magnetic insulating media with permittivity ϵ and $\vartheta = 0$. The red dashed line corresponds to the LH and the purple solid line describes the UH. The scale is normalized by multiplying $dP/d\Omega$ by $8\pi/n\omega^4 p^2$.

The result for our dipole \mathbf{p} is

$$\begin{aligned} \frac{dP}{d\Omega} = \frac{n\omega^4 p^2}{8\pi} \sin^2 \theta \left\{ 1 + \text{sgn}^2(\cos \theta) \frac{\tilde{\theta}^4}{(4n^2 + \tilde{\theta}^2)^2} + \text{sgn}^2(\cos^2 \theta) \frac{4n^2 \tilde{\theta}^2}{(4n^2 + \tilde{\theta}^2)^2} \right. \\ \left. + \frac{2\tilde{\theta}^2}{4n^2 + \tilde{\theta}^2} \text{sgn}(\cos \theta) \cos \left[\tilde{k}_0 z_0 (|\cos \theta| + \cos \theta) \right] \right\}. \end{aligned} \quad (63)$$

Since $\text{sgn}^2(\cos \theta) = \text{sgn}^2(\cos^2 \theta)$, the factorization of the second and third terms in the right-hand side of Eq. (63) yields the simplification

$$\left[\frac{\tilde{\theta}^4}{(4n^2 + \tilde{\theta}^2)^2} + \frac{4n^2 \tilde{\theta}^2}{(4n^2 + \tilde{\theta}^2)^2} \right] = \frac{\tilde{\theta}^2}{4n^2 + \tilde{\theta}^2} \equiv \Upsilon, \quad (64)$$

that cancels the dependence upon $\tilde{\theta}^4$, which would be naively expected when taking the square of the norm of the electric field in Eqs. (39) and (40). Then, Eq. (63) reduces to

$$\frac{dP}{d\Omega} = \frac{n\omega^4 p^2}{8\pi} \sin^2 \theta \left\{ 1 + \Upsilon \text{sgn}^2(\cos \theta) + 2\Upsilon \text{sgn}(\cos \theta) \cos \left[\tilde{k}_0 z_0 (|\cos \theta| + \cos \theta) \right] \right\}. \quad (65)$$

Some comments regarding this angular distribution are now in order. The expression (65) is an even function of the MEP $\tilde{\theta}$ as well as of the angle θ . Furthermore, the last term in Eq. (65) arises from the interference between the two different phases exhibited by the electric field in Eq. (39) and could or could not contribute depending on the sign of $\cos \theta$. Also the angular distribution is independent of ϕ , as required by the azimuthal symmetry of the problem.

At this stage it is important to emphasize that our result in Eq. (65) shows that Υ sets the scale in the magnitude of the power radiated in the region \mathcal{V}_1 . This parameter has the relevant property of being bounded within the interval $0 < \Upsilon < 1$, independently of the values which $\tilde{\theta}$ and n might take. This will severely constrain the response of the ϑ -medium with respect to the output produced by an electric dipole in an infinite media with refraction index n . We refer to the latter reference setup as the standard electrodynamics (SED) case, which is obtained setting $\tilde{\theta} = 0$ in Eq. (65) yielding the angular distribution [37]

$$\frac{dP_{\text{ED}}}{d\Omega} = \frac{n\omega^4 p^2}{8\pi} \sin^2 \theta, \quad (66)$$

whose polar graph is shown in Fig. 3.

Now, we analyze the angular distribution of the radiated power (65) for the Case (–) discussed in Sec. IIIB1, when the electric field has a single phase. Making this choice in Eq. (65), we obtain

$$\frac{dP_{(-)}}{d\Omega} = \frac{n\omega^4 p^2}{8\pi} \sin^2 \theta (1 - \Upsilon). \quad (67)$$

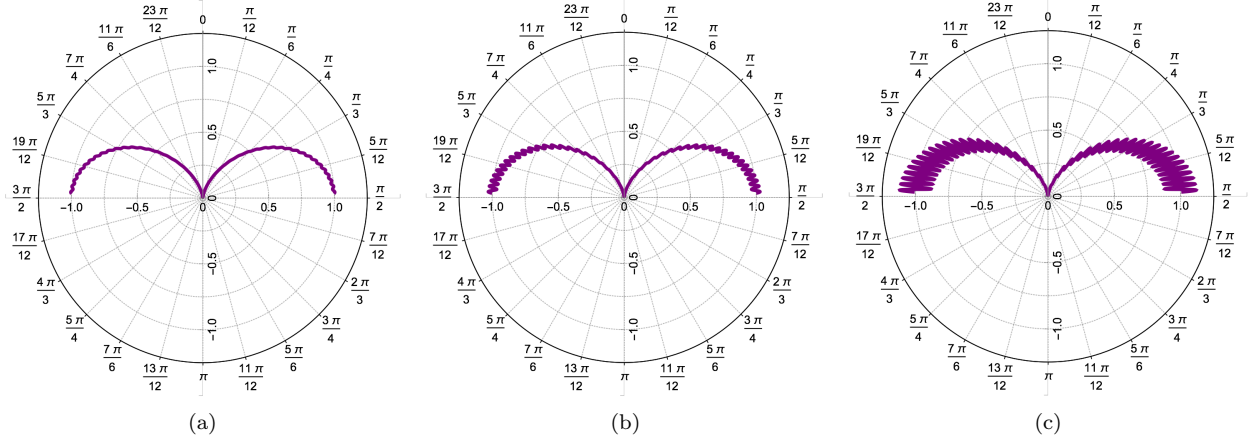


Figure 4: Angular distribution of the radiated power $dP_{(+)} / d\Omega$. (a) Polar plot with $\tilde{\theta} = 0.22$, $n = 1.87$, (b) Polar plot with $\tilde{\theta} = 0.5$, $n = 2$. (c) Polar plot with $\tilde{\theta} = 1$, $n = 2$. The scale is normalized by multiplying $dP_{(+)} / d\Omega$ by $4\pi / \omega^4 p^2$. The remaining parameters $\omega = 1.5 \text{ eV}$, $r = 667 \text{ eV}^{-1}$, $z_0 = 25 \text{ eV}^{-1}$ are common to this and all subsequent figures.

Notice that the factor $(1 - \Upsilon) = 4n^2 / (4n^2 + \tilde{\theta}^2)$ is always positive which confirms a basic property of the radiated power. We observe that the angular dependence of the radiated power remains unchanged with respect to the SED case in Eq. (66). Nevertheless, the magnitude of the radiation turns out to be smaller for a fixed angle, which provides a fundamental difference with respect to this reference setup. Surprisingly, in the highly hypothetical situation where $\Upsilon \rightarrow 1$, the radiation in the LH would be completely canceled i.e. the setup approaches to a perfect mirror.

On the other hand, for the Case (+), when the electric field includes two different phases, we obtain the angular distribution

$$\frac{dP_{(+)}}{d\Omega} = \frac{n\omega^4 p^2}{8\pi} \sin^2 \theta \left[1 + \Upsilon + 2\Upsilon \cos \left(2\tilde{k}_0 z_0 \cos \theta \right) \right], \quad (68)$$

which present additional contributions to the angular distribution with respect to those in SED. They arise from the last term in Eq. (68), which is produced by the interference between the two different phases of the electric field that can be traced back to $f_{\parallel}^+(\theta, z_0, \omega)$ in Eq. (41). Furthermore, as opposed to the previous case, the angular distribution now depends explicitly on the dipole position z_0 . Let us observe that the minimum value -1 of $\cos(2\tilde{k}_0 z_0 \cos \theta)$ produces the factor $(1 - \Upsilon)$ in the square bracket, which was discussed above.

The behavior of the angular distribution (68) is shown in Fig. 4. In each case, the electric dipole is located at $z_0 > 0$ and the interface corresponds to the line $(3\pi/2 - \pi/2)$ defining $z = 0$. Let us recall that we consider both media to be non-magnetic and having the same permittivity ϵ . The Fig. 4a is plotted for the ϑ -medium TbPO_4 with $n = 1.87$ [52] and $\tilde{\theta} = 0.22$ [53]. After comparing with Fig. 3 we appreciate only weak signals of interference. The Fig. 4b corresponds to an hypothetical material with $\tilde{\theta} = 0.5$ and $n = 2$. Finally, in Fig. 4c we see a clear enhancement in the interference pattern for our electric dipole radiating in front of an another hypothetical material with $\tilde{\theta} = 1$ and $n = 2$. An increasing value of the parameter $\tilde{\theta}$ in Fig. 4 makes evident the interference effects, which are expected to be more pronounced in the vicinity of $\theta = \pi/2$ where the last term in Eq. (68) oscillates maximally.

A qualitative interpretation for the radiation patterns described above can be given by extending to the time depending case the description of the static fields produced by a point charge located in front of a magnetoelectric medium in terms of electric and magnetic images presented in detail in Ref. [54]. It is worth mentioning that the image method for frequency dependent sources has been already discussed in Ref. [40] for dipole emission near planar interfaces with different permittivities and we assume that it is valid in the quasi-static approximation. Also we recall the basic dictum of the image method which forbids us to use the contribution of the images to calculate the electromagnetic fields in the same region where the images are located, since they are not real sources of the field. In this way, the full description of the MEE of a dipole located in front of a planar medium includes electric and magnetic image dipoles represented by a superposition of the Figs. (5a) and (5b). Such images contribute to the electric field with terms proportional to $\tilde{\theta}$ and $\tilde{\theta}^2$. Nevertheless, we present them separately to correctly identify the contributions from the source and the images in each case. Let us first deal with the Case (−), which corresponds to the situation when the electric dipole and the observer are in different semi-spaces, i.e. the dipole is located at $\mathbf{r}_0 = (0, 0, z_0)$ with $z_0 > 0$ and the observer's angle θ is in the LH. The MEE is mimicked by introducing an image

dipole \mathbf{p}' and an image magnetic dipole \mathbf{m} located at \mathbf{r}_0 , i.e. in the same semi-space and in the same position of the electric dipole \mathbf{p} (See Fig.5a). So, the observer will measure the same phase of the radiation from \mathbf{p} , \mathbf{p}' and \mathbf{m} , which is given by choosing $|\cos \theta| = -\cos \theta$ in the phase of the electric field (39). This sign choice affects the angular distribution (65) by canceling the interference term, as Eq. (67) shows. Therefore, the angular dependence of the radiation that the observer detects will not present a substantial difference from that of standard electrodynamics (SED). Let us recall that we have chosen the two non-magnetic media having the same permittivity, which eliminates the optical refraction and reflection phenomena when passing from one magnetoelectric medium to the other.

On the other hand, the Case (+) can be understood in a similar way. Here both objects, electric dipole and observer, are in the same semi-space and the observer's angle θ is in the UH. Again we emulate the MEE by inserting an image dipole \mathbf{p}' and the same image magnetic dipole \mathbf{m} [54], both localized at $-\mathbf{r}_0$ (See Fig.5b). In this way, the observer will detect radiation with two different phases: one from the source electric dipole and another, proportional to $\tilde{\theta}$ and $\tilde{\theta}^2$, from the image objects \mathbf{p}' and \mathbf{m} , which corresponds to the choice $|\cos \theta| = +\cos \theta$ in the phase of the electric field (39). The plus sign selection impacts significantly the angular distribution (65) because the interference term is now non-zero and contributes to observable quantities as shown in Eq. (68) together with Fig. 4. This interference arises between the radiation coming from bottom to top, generated by the image objects, and the direct signal from the dipole source. By contrast with the former case, this will generate a different angular dependence in the UH when compared with the electric dipolar radiation of electrodynamics shown in Fig. 3. In order to know how good is the proposed explanation in terms of image charges, one could try to obtain the expression (39) for the electric field in the far-field region \mathcal{V}_1 by superposing the contributions from the source electric dipole \mathbf{p} , the image electric dipole \mathbf{p}' and that produced by a magnetic dipole \mathbf{m} , with magnitudes $p, p' = \tilde{\theta}^2 p / (4n^2 + \tilde{\theta}^2)$ and $m = 2\tilde{\theta} p / 4n^2 + \tilde{\theta}^2$, respectively, using the standard formulas for each source [54]. Nevertheless, a careful analysis of the interpretation using the image method in time-dependent systems is required, in particular regarding on how the retardation should be correctly taken into account. In this way, a further elucidation of the above interpretation of the electric dipolar radiation in our case is beyond the scope of the present manuscript and it is postponed for a future work. As it is well known, image charges are only useful mathematical tools in the description of electromagnetic phenomena and do not represent physically existing entities. In our case, the physical response of the medium is produced by the time varying electric charge densities and Hall currents induced at the interface Σ due to the MEE.

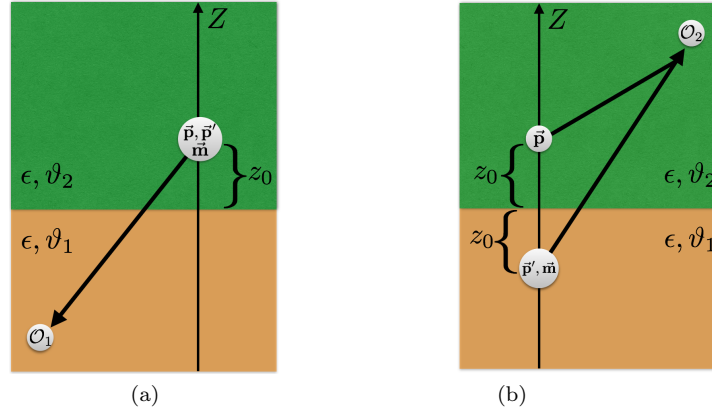


Figure 5: (a) Illustration of the Case (-), where the radiation (black thick arrows) has a single phase, which is the one of standard ED, when the observer \mathcal{O}_1 is in a different semi-space with respect to the dipole \mathbf{p} at z_0 . (b) In the Case (+) (observer \mathcal{O}_2 in the same semi-space of the dipole) the radiation seen by \mathcal{O}_2 includes two phases: the one arising from \mathbf{p} at z_0 and the other that comes from the images \mathbf{p}' and \mathbf{m} at $-z_0$. Recall that we have two non-magnetic medium with $\epsilon_1 = \epsilon_2$, which yield no refraction at the interface.

C. Power radiated in the region \mathcal{V}_1

In order to compare the magnitude of the radiation in the ϑ -medium with respect to the SED case it is convenient to introduce what we call the enhancement factor \mathcal{R}_{\pm} defined as $\mathcal{R}_{\pm} = 2P_{\pm}/P_0$, where $P_0 = n\omega^4 p^2/3$ is the total power radiated by an electric dipole in the SED case [37].

Next we calculate the power radiated for the angular distributions (67) and (68) in the region \mathcal{V}_1 . Let us begin with the angular distribution of the Case (-) given by Eq. (67). Integrating over the solid angle Ω for $\theta \in (\theta_0^L, \pi]$

and $\phi \in [0, 2\pi]$, we find the radiated power

$$P_{(-)} = \frac{P_0}{2} (1 - \Upsilon) \left[1 + \frac{9}{8} \cos \theta_0^{LH} - \frac{1}{8} \cos 3\theta_0^{LH} \right]. \quad (69)$$

A good estimation of the enhancement factor is obtained writing $\theta_0 = \pi/2 + \xi_0$ and recalling that $\xi_0 < 1$. We obtain

$$\mathcal{R}_{(-)} = (1 - \Upsilon) \left(1 + \frac{3\xi_0}{2} \right). \quad (70)$$

which can be larger (smaller) than one according to $\Upsilon < 3\xi_0/2$ ($\Upsilon > 3\xi_0/2$), respectively. In the hypothetical limit $\tilde{\theta} \gg 2n$ we have $\Upsilon = 1$ and there is no radiated power in the LH, which tells us that the setup behaves like a perfect mirror.

Now, we repeat the calculation with the angular distribution of the Case (+) given by Eq. (68), which is more interesting. After integrating over the solid angle Ω for $\theta \in [0, \theta_0^{UH}]$, the power radiated $P_{(+)}$ is

$$\begin{aligned} P_{(+)} = & \frac{P_0}{2} (1 + \Upsilon) \left[1 - \frac{9}{8} \cos \theta_0^{UH} + \frac{1}{8} \cos 3\theta_0^{UH} \right] \\ & + \frac{P_0}{2} 3\Upsilon \left\{ \frac{\sin(2\kappa)}{4\kappa^3} - \frac{\cos(2\kappa)}{2\kappa^2} + \frac{\cos \theta_0^{UH} \cos(2\kappa \cos \theta_0^{UH})}{2\kappa^2} \right. \\ & \left. - \frac{[1 + \kappa^2 - \kappa^2 \cos(2\theta_0^{UH})] \sin(2\kappa \cos \theta_0^{UH})}{4\kappa^3} \right\}, \quad \kappa \equiv \tilde{k}_0 z_0. \end{aligned} \quad (71)$$

The main difference with respect to the power radiated in the LH is that now $P_{(+)}$ depends on the position of the dipole through the variable κ . The power radiated $P_{(+)}$ is positive definite and due to the term in braces we expect to find new effects in comparison with the previous Case (-). Moreover, from Eq. (71) and retaining n and ω fixed we find the following interesting limits for z_0

$$P_{(+)}(z_0 \rightarrow \infty) = \frac{P_0}{2} (1 + \Upsilon) \left(1 - \frac{9}{8} \cos \theta_0^{UH} + \frac{1}{8} \cos 3\theta_0^{UH} \right), \quad (72)$$

$$\begin{aligned} P_{(+)}(z_0 \rightarrow 0) = & \frac{P_0}{2} (1 + 3\Upsilon) \left(1 - \frac{9}{8} \cos \theta_0^{UH} + \frac{1}{8} \cos 3\theta_0^{UH} \right) \\ & + \frac{P_0}{2} \frac{2}{5} \Upsilon \kappa^2 \left(5 \cos^3 \theta_0^{UH} - 3 \cos^5 \theta_0^{UH} - 2 \right), \quad \kappa \ll 1. \end{aligned} \quad (73)$$

The Eq. (73) tell us that there are no divergences in Eq. (71) when the electric dipole is very close to the interface. Since for all practical purpose θ_0^{UH} is very close to $\pi/2$, we obtain a very good approximation of $P_{(+)}$ in the intricate Eq. (71) by setting $\theta_0^{UH} = \pi/2$, which yields the simplified expression

$$P_{(+)} = \frac{P_0}{2} \left(1 + \Upsilon \left[1 + \frac{3 \sin(2\kappa)}{4\kappa^3} - \frac{3 \cos(2\kappa)}{2\kappa^2} \right] \right). \quad (74)$$

As we can calculate from Eq. (74), the enhancement factor $\mathcal{R}_{(+)} = 2P_{(+)}/P_0$ has the following properties. The maximum occurs when the dipole is at the interface ($\kappa = 0$) and yields $\mathcal{R}_{(+)}^{\max} = (1 + 3\Upsilon)$. Also we found an absolute minimum located at $\kappa \approx 2.88$ where $\mathcal{R}_{(+)}^{\min} = (1 + 0.83 \Upsilon)$. The limit for very large κ is $\mathcal{R}_{(+)}^{\infty} = (1 + \Upsilon)$. In the Fig. 6 we plot the ratio $P_{(+)}/P_0$ in the approximation of Eq. (74), as a function of κ for different choices of the parameter Υ , which provides a qualitative confirmation of the behavior of $\mathcal{R}_{(+)}$ discussed above.

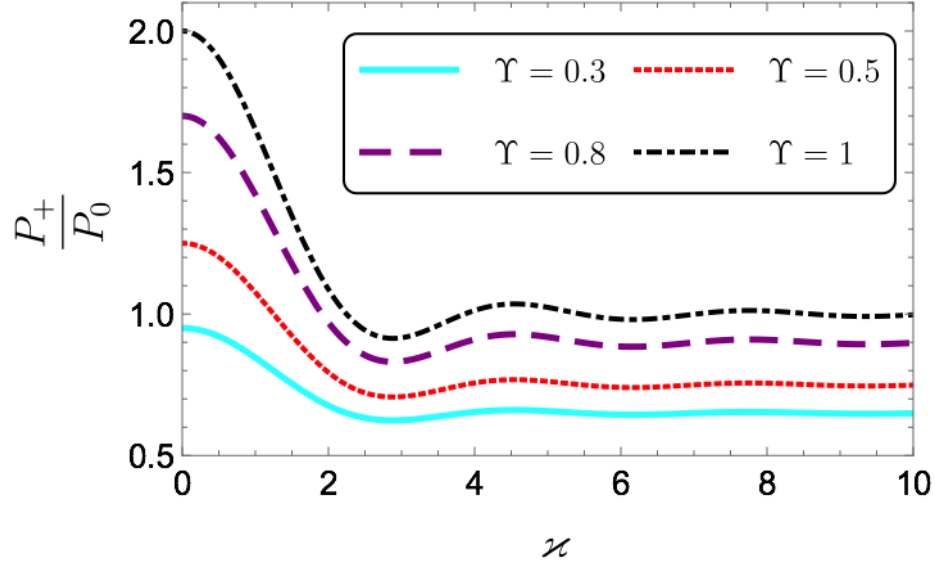


Figure 6: Plot of $P_{(+)}/P_0$ as a function of κ for different choices of Υ . The enhancement factor is $\mathcal{R}_{(+)} = 2P_{(+)}/P_0$.

D. Energy transport in the region \mathcal{V}_2

In this subsection we discuss the energy flux in the region \mathcal{V}_2 due to the spherical and surface waves in Eq. (60). As pointed out in Ref. [49], the separation of the electric field (60) in these two components is not significant since they do not constitute independent solutions of Maxwell equations. Recalling Eq. (61) for the time-averaged Poynting vector $\langle \mathbf{S} \rangle$ we obtain

$$\langle \mathbf{S} \rangle_{\mathcal{V}_2}^{UH} = \hat{\mathbf{n}} \frac{np^2\omega^4}{8\pi} \left\{ \frac{1}{r^2} \left[1 + \frac{4\tilde{\theta}^2 n^2}{(4n^2 + \tilde{\theta}^2)^2} \right] + \frac{\omega^{1/2}}{r^{3/2}} \frac{\tilde{\theta}^2}{4n^2 + \tilde{\theta}^2} \sqrt{n\pi} \xi \right\} + \mathcal{O}(\xi^2), \quad (75)$$

$$\langle \mathbf{S} \rangle_{\mathcal{V}_2}^{LH} = \hat{\mathbf{n}} \frac{np^2\omega^4}{8\pi} \left\{ \frac{1}{r^2} \left[1 + \frac{4\tilde{\theta}^2 n^2}{(4n^2 + \tilde{\theta}^2)^2} \right] - \frac{\omega^{1/2}}{r^{3/2}} \frac{\tilde{\theta}^2}{4n^2 + \tilde{\theta}^2} \sqrt{n\pi} \xi \right\} + \mathcal{O}(\xi^2), \quad (76)$$

to first order in ξ . In the above linear expansion we require

$$n\omega z_0 \xi \ll 1. \quad (77)$$

We observe that these fluxes are independent of the position of the dipole. In Eqs. (75) and (76) we encounter two different terms: one modulated by r^{-2} which contains the energy flux coming from the spherical wave contribution, and another one proportional to $r^{-3/2}$ that encodes the interference between the spherical and surface waves. The contribution of the surface wave itself is of order ξ^2 which we have consistently neglected in our approximation.

Two remarks are now in order: (i) For a fixed set of parameters, Eqs. (75) and (76) yields $\langle \mathbf{S} \rangle_{\mathcal{V}_2}^{UH} - \langle \mathbf{S} \rangle_{\mathcal{V}_2}^{LH} > 0$. (ii) The full expression for the energy flux must be positive definite, but we are dealing only with a linear approximation in Eq. (76). This forces us to establish an additional bound for the validity of our results. The dangerous contribution is in $\langle \mathbf{S} \rangle_{\mathcal{V}_2}^{LH}$, where the relative minus sign might produce a negative value. Recalling that $\xi_0 = \sqrt{2/(n\omega r)}$, defined after Eq. (37), we rewrite the resulting condition from Eq. (76) as

$$\frac{\xi}{\xi_0} < \frac{1}{\sqrt{2\pi}} \frac{(4n^2 + \tilde{\theta}^2)^2 + 4n^2\tilde{\theta}^2}{\tilde{\theta}^2(4n^2 + \tilde{\theta}^2)} = \frac{1}{\sqrt{2\pi}} \frac{1 + \Upsilon - \Upsilon^2}{\Upsilon} \equiv Q(\Upsilon), \quad \tilde{\theta} \neq 0, \quad (78)$$

which can be expressed only in terms of Υ . The function $Q(\Upsilon)$ is a decreasing function having its minimum value $Q(\Upsilon = 1) = 0.40$, which means that for any value $\xi/\xi_0 < 0.40$, the energy fluxes are always positive in the whole range $0 < \Upsilon < 1$. On the contrary, when $0.40 < \xi/\xi_0 \equiv \zeta < 1$ we have to determine the maximum allowed value Υ_{\max} by solving $Q(\Upsilon_{\max}) = \zeta$, so that the energy fluxes are positive only in the range $0 < \Upsilon < \Upsilon_{\max}$. Let us observe that

ϑ -medium	n	$\tilde{\theta}$	Υ	$\langle S \rangle^{UH}$ [eV ⁴]	$\langle S \rangle^{LH}$ [eV ⁴]	$\langle S \rangle^{SED}$ [eV ⁴]
TlBiSe ₂	2	11α	4.0×10^{-4}	6.64	6.64	6.63
TbPO ₄	1.87	0.22	3.5×10^{-3}	6.21	6.21	6.18
Hyp. I	2	0.5	1.5×10^{-2}	6.74	6.73	6.63
Hyp. II	2	1	5.9×10^{-2}	7.03	6.97	6.63
Hyp. III	2	5	6.1×10^{-1}	8.53	7.89	6.63

Table I: The energy flux very close to the interface ($\xi = 10^{-3}$) between a normal insulator ($n = 2$ (1.87), $\tilde{\vartheta} = 0$, $\mu = 1$) and different magnetoelectrics with the same n and μ . The radiating dipole has $p = 2.71 \times 10^3$ eV⁻¹, $\omega = 1.5$ eV and $z_0 = 25$ eV⁻¹. The observer distance is $r = 667$ eV⁻¹.

the lowest values observed for $\tilde{\theta}$ are of the order of the fine structure constant $\alpha = 1/137$, which effectively replaces the theoretical lower limit $\Upsilon = 0$ by the more realistic one $\Upsilon_{\min} = 1.3 \times 10^{-5}/n^2$.

Next we perform some numerical estimations of Eq. (76) shown in Table I. There we refer to the setup in Fig. 1 for the case where medium 1 is a regular insulator with $n = 2$ (1.87), $\mu = 1$ and $\vartheta = 0$, while medium 2 corresponds to different magnetoelectric media with the same refraction index and permeability and whose value of $\tilde{\theta}$ is indicated in the third column. The parameters for TlBiSe₂ and TbPO₄ are taken from Refs. [51] and [52, 53], respectively. The remaining entries are hypothetical materials aiming to illustrate the effects of increasing the strength of the MEE. We compare these fluxes with the magnitude of $\langle S \rangle^{SED}$ written in the last column. We recall the dipole characteristics $p = 2.71 \times 10^3$ eV⁻¹ (10^{-21} cm), $\omega = 1.5$ eV, $z_0 = 25$ eV⁻¹ and the observer distance $r = 667$ eV⁻¹. In this case $\xi_0 = 3.2 \times 10^{-2}$. We present the magnitude of the Poynting vector $\langle S \rangle_{\mathcal{V}_2}$ for both hemispheres evaluated at $\xi = 10^{-3}$, which we choose as a representative value satisfying the condition (77) with $n\omega z_0 \xi = 7.5 \times 10^{-2}$, as well as $\xi/\xi_0 = 3.1 \times 10^{-2}$, for $n \approx 2$. This latter number indicates that the condition (76) is fulfilled for all values of Υ in this case.

V. SUMMARY AND CONCLUSIONS

We discuss the radiation produced by a point-like electric dipole oriented perpendicular to and at a distance z_0 from the interface Σ shown in Fig. 1. This interface separates two planar semi-infinite non-magnetic magnetoelectric media with the same permittivity, whose electromagnetic response obeys the modified Maxwell equations (5) and (6) of ϑ -electrodynamics. The choice $\epsilon_1 = \epsilon_2$ is made to highlight and isolate the purely magnetoelectric effects on the radiation, which depend on the parameter $\tilde{\theta} = \alpha(\vartheta_2 - \vartheta_1)/\pi$. In this way, setting $\vartheta_1 = \vartheta_2 = 0$ reduces our setup to an infinite media with permittivity ϵ and no interface.

As a consequence of a careful calculation of the far-field approximation in the electric field we discover the additional generation of axially symmetric cylindrical surface waves close to the interface, as shown in Eqs. (60). The analysis of the surface waves leads us to introduce what we call a discarding angle θ_0 , which allows to separate the far-field approximation in two regions according to the magnitude of the surface wave contribution. We introduce two discarding angles θ_0^{UH} and θ_0^{LH} , defined in Eq. (28) and shown in Fig. 2, which enable us to distinguish two separate regimes: i) the region \mathcal{V}_1 , ($0 < \theta < \theta_0^{UH}$, $\theta_0^{LH} < \theta < \pi$), where only the spherical waves are taken into account, thus neglecting the surface contribution and ii) the region \mathcal{V}_2 , ($\theta_0^{UH} < \theta < \theta_0^{LH}$), where both the surface and the spherical waves must be taken into account.

Due to the presence of the ϑ -media we find modifications in the angular distribution of the radiation given by Eq. (65) and illustrated in Fig. 4. Noticeable interference effects are manifest in the upper hemisphere when the observer is in the same region of the dipole. On the contrary, no interference occurs when the observer and the dipole are in the same region, in which case the angular distribution looks similar to that of dipole in a homogeneous media, except for important changes in its magnitude. Such different interference effects saying that the system distinguishes whether the electric dipole and the observer are in the same semi-space or not, correspond to the Cases (+) and (−) respectively, and were discussed in Sec. IV B.

Starting from the far-field approximation of the electric field we have correctly identified the Fresnel coefficients at the interface by making use of the angular spectrum representation developed in Ref. [40] as well the work in Ref. [50] dealing with wave propagation in layered topological insulators.

The modifications of the angular distribution in the region \mathcal{V}_1 produce new expressions for the total radiated power $P_{(\pm)}$, which were calculated in Eqs. (69) and (71). The result P_- for the lower hemisphere is independent of the location z_0 of the dipole, which cancels in Eq. (65) since $|\cos \theta| + \cos \theta = 0$ in this case. The result shows a behavior

similar to the SED case, but modulated by two amplitudes. The amplitude depending on the discarding angle θ_0^{LH} is very close to one, because for all practical purposes $\theta_0^{LH} = \pi/2$. The second amplitude depends on Υ and induces an unexpected behavior yielding an enhancement factor $\mathcal{R}_{(-)}$ that can be less than one in some cases. Further, in the limiting case when $\Upsilon \rightarrow 1$ the radiation in the lower hemisphere would be completely canceled, such that the setup behaves as a perfect mirror. The result for $P_{(+)}$ is more intricate since the dependence upon z_0 now survives in the angular distribution (65). Again, the discarding angle is very close to $\pi/2$ and we take this approximation to obtain some general features of the enhancement factor. We find the maximum value $\mathcal{R}_{(+)} = 1 + 3\Upsilon$, when the dipole is located at the interface ($z_0 = 0$). In the limit $\varkappa = n\omega z_0$ very large we have $\mathcal{R}_{(+)} \rightarrow 1 + \Upsilon$. Also we find an absolute minimum at $\varkappa \approx 2.88$ where $\mathcal{R}_{(+)} = 1 + 0.83\Upsilon$. Thus, in this case we have an enhancement factor larger than one, which nevertheless is limited to the maximum value of $\mathcal{R}_{(+)}^{\max} = 4$, independently of our choice of the parameters $\tilde{\theta}$ and n of the medium. In Fig. 6 we plot the ratio $P_{(+)}/P_0$ as a function of \varkappa , for different choices of Υ .

In the region \mathcal{V}_2 , where the surface waves arise, the effect of the ϑ -medium is again codified in the parameter Υ . The surface waves are present in the whole interval $0 < \xi < \xi_0$ but our linear approximation in ξ is only valid when $\xi \ll \xi_0$. As expected, the effects of the magnetoelectric become more evident for large $\tilde{\theta}$. The fluxes in the upper and lower hemispheres are larger than in the SED configuration and the excess of radiation in the upper hemisphere with respect to the lower hemisphere is evident in Table I.

In order to stress their similarities and differences we give some comparison between the dipolar radiation studied in this work which includes a magnetoelectric medium, and that produced in the presence of two standard insulators with a planar interface and different permittivities $\epsilon(\mathbf{x}) = \Theta(z)\epsilon_2 + \Theta(-z)\epsilon_1$ with $\epsilon_1 \neq \epsilon_2$ and $\vartheta_1 = \vartheta_2 = 0$. In the latter case the radiation of a vertically oriented dipole picks up only the TM polarization as shown in Refs. [40, 46]. In our case we have identified these contributions to the electric field through the corresponding transmission ($T_{TM, TM}$) and reflection ($R_{TM, TM}$) coefficients in Eqs. (58) and (59). However, due to the magnetoelectric effect, the electric field gets an additional input arising from the mixing of TM and TE modes described by the reflection coefficient $R_{TE, TM}$ in Eq. (58). While in purely dielectric configuration these coefficients have an angular dependence, in our case they turn out to be constants depending only on the parameters of the media. This is a consequence of our choice $\epsilon_1 = \epsilon_2$, which forbids the existence of reflection and refraction at the interface. On the other hand, both configurations share the generation of axially symmetric cylindrical surface waves at the interface of the two media, as shown in Sec. IIIB 2 of the present work. Again, in our case the physical origin of such surface waves relies on the change in the magnetoelectric polarizability across the two media and not because of a difference in the permittivity constant as it happens in the purely dielectric configuration.

Let us emphasize once again that our methods can be applied to any material whose macroscopic electromagnetic response is described by ϑ -ED. Generally speaking, the parameter $\tilde{\alpha} \equiv \alpha\vartheta/\pi$ (in Gaussian units) which sets the scale for the magnetoelectric effect via the constitutive relations (4), and which quantifies the strength of the corrections with respect to standard ED, is very small. Besides those values previously mentioned in the text, some typical values are: 2.8×10^{-2} for MgO/Fe [62] and 7.2 for Gd₂O₃/Co [63]. Nonetheless, the search for a giant magnetoelectric polarizability continues recently in composite materials reaching values as high as 9.0×10^2 for BaTiO₃/Co₆₀Fe₄₀, for example [64]. In this way, the confirmation of the new effects discussed in this work could be soon within the scope of present day technology.

ACKNOWLEDGMENTS

OJF has been supported by the postdoctoral fellowship CONACYT-770691 and the doctoral fellowship CONACYT-271523. OJF and LFU acknowledge support from the CONACYT project #237503 as well as the project DGAPA-UNAM-IN103319. LFU acknowledges also support from the project CONACyT (México) # CF-428214. LFU and OJF thank Professor Rubén Barrera, Prof. Hugo Morales-Técutl, Dr. Alberto Martín-Ruiz and Dr. Omar Rodríguez-Tzompantzi for useful discussions and suggestions.

Appendix A: The electromagnetic potential and the integrals \mathcal{H} , \mathcal{I} and \mathcal{J}

In this appendix we derive the electromagnetic potential A_μ due to the vertically oriented dipole, together with the integrals in Eqs. (21), (22) and (23) of Sec. III A. The procedure is based on the Appendix of Ref. [44]. To this aim we begin from the expression (12) in the frequency-space and from the current defined in Eq. (17). Let us start with

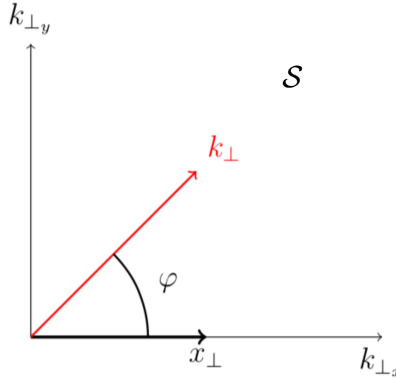


Figure 7: The vectors $\mathbf{k}_\perp = \{k_{\perp x}, k_{\perp y}\}$ and \mathbf{x}_\perp in the coordinate system \mathcal{S} .

the component $A^0(\mathbf{x}; \omega)$, which takes the form

$$A^0(\mathbf{x}; \omega) = -\frac{ip}{\epsilon} \int dz' \int_0^\infty \frac{k_\perp dk_\perp}{\sqrt{\tilde{k}_0^2 - k_\perp^2}} J_0(k_\perp \rho) e^{i\sqrt{\tilde{k}_0^2 - k_\perp^2}|z-z'|} \delta'(z' - z_0) \\ - \frac{i}{\epsilon} \frac{\tilde{\theta}^2 p}{4n^2 + \tilde{\theta}^2} \int dz' \int_0^\infty \frac{k_\perp^3 dk_\perp}{(\tilde{k}_0^2 - k_\perp^2)^{3/2}} J_0(k_\perp \rho) e^{i\sqrt{\tilde{k}_0^2 - k_\perp^2}(|z|+|z'|)} \delta'(z' - z_0), \quad (\text{A1})$$

after making the convolution of the GF (16) with the current (17). In obtaining the above relation we have expressed the area element $d^2\mathbf{k}_\perp = k_\perp dk_\perp d\varphi$ in polar coordinates and we have chosen the $k_{\perp x}$ axis in the direction of the vector $\mathbf{x}_\perp = (x, y, 0)$. This defines the coordinate system \mathcal{S} to be repeatedly used in the following, and shown in Fig. 7. Next we write $\mathbf{k}_\perp \cdot \mathbf{x}_\perp = k_\perp \rho \cos \varphi$ with $\rho = \|\mathbf{x}_\perp\| = \sqrt{x^2 + y^2}$ and recall that the angular integral of $\exp(ik\rho \cos \varphi)$ provides a representation of the Bessel function $J_0(k_\perp \rho)$ [55]. The first integral in Eq. (A1) can be carried out by recalling the Sommerfeld identity [6, 9, 45]

$$i \int_0^\infty \frac{k_\perp dk_\perp}{\sqrt{\tilde{k}_0^2 - k_\perp^2}} J_0(k_\perp R_\perp) e^{i\sqrt{\tilde{k}_0^2 - k_\perp^2}|z-z'|} = \frac{e^{i\tilde{k}_0 R}}{R}, \quad (\text{A2})$$

where $R = \sqrt{\rho^2 + (z - z')^2}$. Then, we impose the coordinate conditions appropriate to the far-field approximation

$$\|\mathbf{x}\| \gg \|\mathbf{x}'\|, \quad R_\perp = \|(\mathbf{x} - \mathbf{x}')_\perp\| \simeq \|\mathbf{x}_\perp\| = \rho, \quad |z - z'| \simeq |z|, \quad (\text{A3})$$

which yields the well-known result of standard ED, $e^{i\tilde{k}_0 R}/R \rightarrow e^{i\tilde{k}_0(r - \hat{\mathbf{n}} \cdot \mathbf{x}')}/r$, with $\hat{\mathbf{n}}$ being a unit vector in the direction of \mathbf{x} and where $\|\mathbf{x}\| = r$ [37, 41]. Substituting this approximation into the first integral of Eq. (A1) and integrating $\delta'(z' - z_0)$ we obtain

$$A^0(\mathbf{x}; \omega) = -\frac{p}{\epsilon} i\tilde{k}_0 \cos \theta \frac{e^{i\tilde{k}_0(r - z_0 \cos \theta)}}{r} - \frac{1}{\epsilon} \frac{\tilde{\theta}^2 p}{4n^2 + \tilde{\theta}^2} \int \frac{k_\perp^3 dk_\perp}{\tilde{k}_0^2 - k_\perp^2} J_0(k_\perp \rho) e^{i\sqrt{\tilde{k}_0^2 - k_\perp^2}(|z|+z_0)}. \quad (\text{A4})$$

Therefore, after making $n^2 = \epsilon$ and identifying the integral \mathcal{H} defined in Eq. (21) we find the expression (18). For convenience we proceed now to calculate simultaneously the components $A^1(\mathbf{x}; \omega)$ and $A^2(\mathbf{x}; \omega)$, which can be written together as

$$A^a(\mathbf{x}; \omega) = -\frac{2\tilde{\theta}p}{4n^2 + \tilde{\theta}^2} \epsilon^a{}_{0b3} I_b(\mathbf{x}, z_0; \omega) - \frac{\tilde{\theta}^2 p}{4n^2 + \tilde{\theta}^2} Q_a(\mathbf{x}, z_0; \omega), \quad (\text{A5})$$

where we define the integrals

$$I_a(\mathbf{x}, z_0; \omega) = - \int_0^\infty \frac{k_\perp^2 dk_\perp}{\sqrt{\tilde{k}_0^2 - k_\perp^2}} e^{i\sqrt{\tilde{k}_0^2 - k_\perp^2}(|z|+z_0)} J_0(k_\perp \rho) v_a, \quad (\text{A6})$$

$$Q_a(\mathbf{x}, z_0; \omega) = \int_0^\infty \frac{k_\perp^2 dk_\perp}{\tilde{k}_0^2 - k_\perp^2} e^{i\sqrt{\tilde{k}_0^2 - k_\perp^2}(|z|+z_0)} J_0(k_\perp \rho) v_a, \quad (\text{A7})$$

with $v_a = (\cos \varphi, \sin \varphi, 0)$. Here $a, b = 1, 2$ and $k_a = (\mathbf{k}_\perp, 0)$. Choosing the coordinate system \mathcal{S} previously introduced in Fig. 7, I_a and Q_a are calculated obtaining $I_2 = 0$ and $Q_2 = 0$, which tells us that both vectors \mathbf{I} and \mathbf{Q} in the subspace parallel to the interface point in the direction of \mathbf{x}_\perp , where $\{x^1, x^2\} = \mathbf{x}_\perp$. Thus we can write

$$\mathbf{I}(\mathbf{x}, z_0; \omega) = \mathbf{x}_\perp \frac{i}{\rho} \frac{\partial}{\partial \rho} \int_0^\infty \frac{k_\perp dk_\perp}{\sqrt{\tilde{k}_0^2 - k_\perp^2}} J_0(k_\perp \rho) e^{i\sqrt{\tilde{k}_0^2 - k_\perp^2}(|z|+z_0)}, \quad (\text{A8})$$

$$\mathbf{Q}(\mathbf{x}, z_0; \omega) = -\mathbf{x}_\perp \frac{i}{\rho} \frac{\partial}{\partial \rho} \int_0^\infty \frac{k_\perp dk_\perp}{\tilde{k}_0^2 - k_\perp^2} J_0(k_\perp \rho) e^{i\sqrt{\tilde{k}_0^2 - k_\perp^2}(|z|+z_0)}, \quad (\text{A9})$$

where we identify the integrals \mathcal{I} and \mathcal{J} previously introduced in Refs. (22) and (23). Plugging the latter forms of \mathcal{I} and \mathcal{J} into Eq. (A5) we find the expression (19). Finally, we will determine the component $A^3(\mathbf{x}; \omega)$, which is given by

$$A^3(\mathbf{x}; \omega) = \omega p \int_0^\infty \frac{k_\perp dk_\perp}{\sqrt{\tilde{k}_0^2 - k_\perp^2}} J_0(k_\perp R_\perp) e^{i\sqrt{\tilde{k}_0^2 - k_\perp^2}|z-z_0|}. \quad (\text{A10})$$

Employing the Sommerfeld identity (A2) together with the far-field approximation (A3) we find Eq. (20).

Appendix B: Evaluating the integrals (21)-(23) by the modified steepest descent method

In this appendix we apply a modified steepest descent method to find the far-field approximation of the integrals \mathcal{H} , \mathcal{I} and \mathcal{J} whose results are given in Eqs. (24)-(26). We closely follow Ref. [15], which provides a detailed account of the general procedure to deal with the steepest descent method for these class of integrals. This Appendix is divided in three sections. In the first one, we will present in full detail the method by solving the integral \mathcal{H} defined in Eq. (21). In the second and third section we present a summary version of the method to compute the integrals \mathcal{J} and \mathcal{I} , respectively.

1. The integral \mathcal{H}

It will prove convenient to rewrite \mathcal{H} in terms of Hankel functions. We start from

$$J_0(x) = \frac{1}{2} \left[H_0^{(1)}(x) + H_0^{(2)}(x) \right], \quad (\text{B1})$$

where $H_0^{(1)}(x)$ and $H_0^{(2)}(x)$ are the Hankel functions, together with the reflection formula $H_0^{(1)}(e^{i\pi}x) = -H_0^{(2)}(x)$ [56], which allows us to extend the integration interval in Eq. (21) to $-\infty$. The result is

$$\mathcal{H}(\mathbf{x}, z_0; \omega) = \frac{1}{2} \oint_{C_{k_\perp}} \frac{k_\perp^3 dk_\perp}{\tilde{k}_0^2 - k_\perp^2} H_0^{(1)}(k_\perp \rho) e^{i\sqrt{\tilde{k}_0^2 - k_\perp^2}(|z|+z_0)}, \quad (\text{B2})$$

where C_{k_\perp} is the so-called Sommerfeld path of integration defined in Fig. 8a, which avoids the branch cuts dictated by the Hankel function $H_0^{(1)}$ and by the square root $\sqrt{\tilde{k}_0^2 - k_\perp^2}$. At this point is worth mentioning that henceforth we will retain some dissipation in the medium ($1 \gg \text{Im}[\tilde{k}_0] > 0$) for convergence purposes and to avoid troublesome questions of convergence that arise when $\text{Im}[\tilde{k}_0] = 0$. This guarantees that $\text{Re} \left[i\sqrt{\tilde{k}_0^2 - k_\perp^2} \right] < 0$, i.e., the exponential argument will be negative implying the rapidly exponential decay that assures the convergence of the integral \mathcal{H} [15].

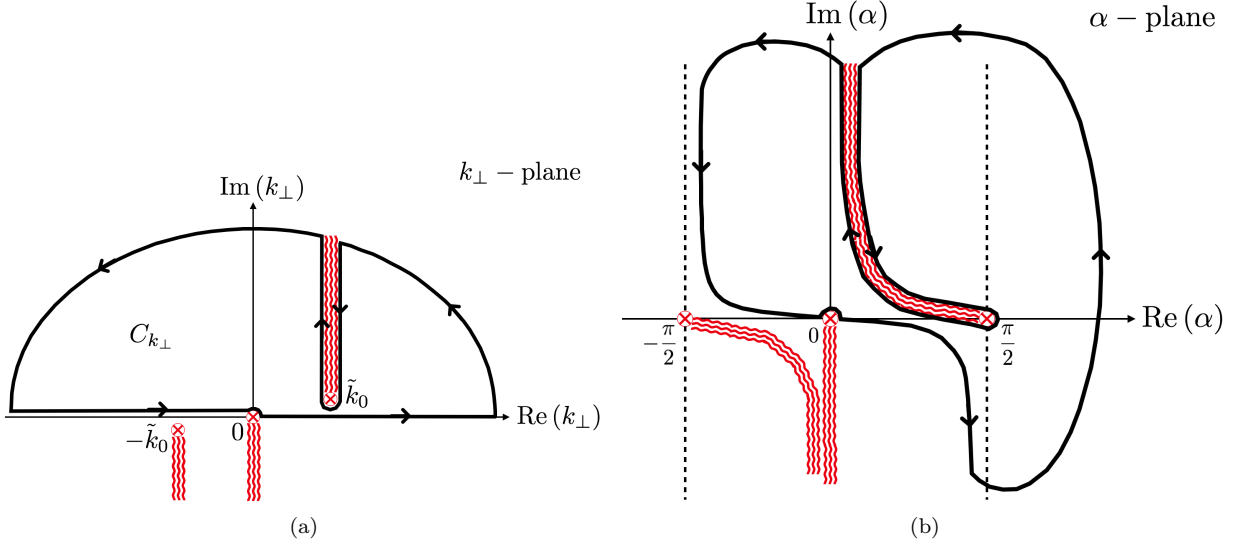


Figure 8: (a) The Sommerfeld path of integration $C_{k_{\perp}}$ in the k_{\perp} -plane showing the branch cuts originating from the branch points $\pm\tilde{k}_0$ and 0. (b) A permissible deformation C_{α} of the path of integration obtained by the transformation $k_{\perp} = \tilde{k}_0 \sin \alpha$. The branch points in the α -plane are $\alpha_{\pm}(\pm\tilde{k}_0) = \pm\pi/2$ and $\alpha(0) = 0$.

First, we apply the conformal transformation $k_{\perp} = \tilde{k}_0 \sin \alpha$ obtaining [15, 49]

$$\mathcal{H}(\mathbf{x}, z_0; \omega) = \frac{\tilde{k}_0^2}{2} \oint_{C_{\alpha}} d\alpha \frac{\sin^3 \alpha}{\cos \alpha} H_0^{(1)}(\tilde{k}_0 \rho \sin \alpha) e^{i\tilde{k}_0 \cos \alpha (|z| + z_0)}. \quad (\text{B3})$$

where C_{α} is given in Fig. 8b. Following Ref. [49], now it is convenient to use the asymptotic expansion of the Hankel function [55]

$$H_0^{(1)}(\tilde{k}_0 \rho \sin \alpha) \sim \sqrt{\frac{2}{\pi \tilde{k}_0 \rho \sin \alpha}} e^{i\tilde{k}_0 \rho \sin \alpha - i\frac{\pi}{4}}, \quad (\text{B4})$$

which is allowed because we are focusing on the far-field approximation required for the analysis of radiation. In this way, we have

$$\mathcal{H}(\mathbf{x}, z_0; \omega) = \tilde{k}_0^2 \sqrt{\frac{1}{2\pi \tilde{k}_0 R_{\perp}}} e^{-i\pi/4} \oint_{C_{\alpha}} d\alpha \frac{\sin^{5/2} \alpha}{\cos \alpha} e^{i\tilde{k}_0 \rho \sin \alpha + i\tilde{k}_0 \cos \alpha (|z| + z_0)}. \quad (\text{B5})$$

For the moment we restrict ourselves only to the UH ($\cos \theta > 0$). The calculation for the LH is sketched after Eq. (B22). So, we write $|z| = r \cos \theta$ and $\rho = r \sin \theta$, i.e., $r = \sqrt{\rho^2 + z^2}$. Thereby, we find

$$\mathcal{H}(\mathbf{x}, z_0; \omega) = \tilde{k}_0^2 \sqrt{\frac{1}{2\pi \tilde{k}_0 r \sin \theta}} e^{-i\pi/4} \oint_{C_{\alpha}} d\alpha \frac{\sin^{5/2} \alpha}{\cos \alpha} e^{i\tilde{k}_0 r \cos(\alpha - \theta) + i\tilde{k}_0 z_0 \cos \alpha}. \quad (\text{B6})$$

Next we determine the saddle-point of (B6) by choosing the stationary phase as only $\varphi(\alpha) = i\tilde{k}_0 r \cos(\alpha - \theta)$, according to Ref. [15]. The saddle-point α_s is determined through $\varphi'(\alpha_s) = 0$, which gives $\alpha_s = \theta$. This yields the full stationary phase to be $i\tilde{k}_0 r \cos \theta$. At this stage, the steepest descent path is specified on the α -plane by demanding the condition

$$\text{Im}[\varphi(\alpha)] = \text{Im}[\varphi(\alpha_s)] \Rightarrow \text{Im}[i\tilde{k}_0 r \cos(\alpha - \theta)] = \text{Im}[i\tilde{k}_0 r] \quad (\text{B7})$$

over C_{α} , as sketched in Fig. 9a.

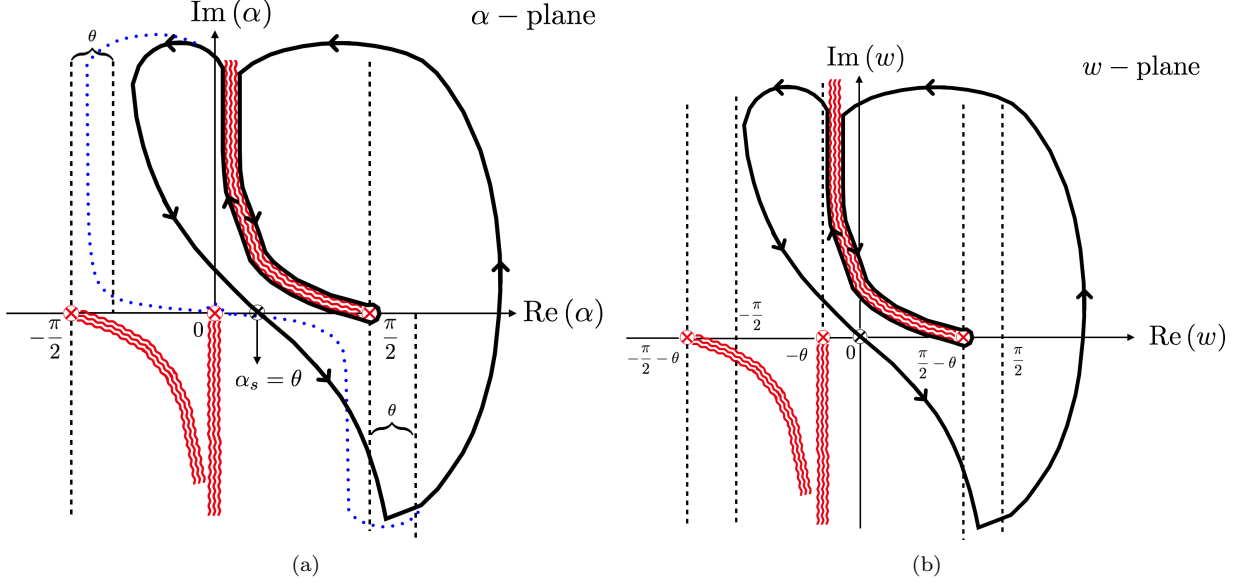


Figure 9: (a) The path of integration C_α with the steepest descent condition (B7) in the α -plane. The path of steepest descent has the asymptotes $\text{Re}(\alpha) = -\pi/2 + \theta$, $\pi/2 + \theta$, and crosses the real axis of the α -plane at the saddle-point $\alpha_s = \theta$. The previous path C_α of Fig. 8b is sketched here in the blue dotted line. (b) The path of integration C_w in the w -plane obtained by the shift $w = \alpha - \theta$. The resulting path of steepest descent now has the asymptotes $\text{Re}(w) = \pm\pi/2$ and crosses the real axis of the w -plane at $w = 0$.

Now we shift the origin to coincide with the saddle point by setting $w = \alpha - \theta$ in \mathcal{H} , which yields

$$\mathcal{H}(\mathbf{x}, z_0; \omega) = \tilde{k}_0^2 \sqrt{\frac{1}{2\pi\tilde{k}_0 r \sin \theta}} e^{-i\pi/4} \oint_{C_w} dw \frac{\sin^{5/2}(\theta + w)}{\cos(\theta + w)} e^{i\tilde{k}_0 r \cos w + i\tilde{k}_0 z_0 \cos(\theta + w)}. \quad (\text{B8})$$

The reparametrized path C_w , shown in Fig. 9b, now satisfies the following steepest descent condition

$$\text{Im} [i\tilde{k}_0 r \cos w] = \text{Im} [i\tilde{k}_0 r]. \quad (\text{B9})$$

The next step is to introduce the conformal transformation [15]

$$\frac{u^2}{2} = \varphi(0) - \varphi(w) = i\tilde{k}_0 r (1 - \cos w), \quad (\text{B10})$$

whose purpose is to map the path of steepest descent into the real axis. This requires the change of variables $\cos w = 1 - u^2/2i\tilde{k}_0 r$ in Eq.(B8), after which we obtain

$$\mathcal{H}(\mathbf{x}, z_0; \omega) = \frac{\tilde{k}_0}{i} \sqrt{\frac{1}{2\pi \sin \theta}} \frac{e^{i\tilde{k}_0 r}}{r} \oint_{C_u} du F_1(u) e^{-u^2/2}, \quad F_1(u) = \frac{\sin^{5/2}[\theta + w(u)] e^{i\tilde{k}_0 z_0 \cos[\theta + w(u)]}}{\cos[\theta + w(u)] \sqrt{1 - \frac{u^2}{4i\tilde{k}_0 r}}}. \quad (\text{B11})$$

The path C_u is sketched in Fig. 10. Then we look at the behavior of $F_1(u)$ and find that it has poles in the u -plane located at u_0 given by

$$\sqrt{1 - \frac{u_0^2}{4i\tilde{k}_0 r}} = 0, \quad \cos[\theta + w(u_0)] = 0. \quad (\text{B12})$$

We will consider only those poles in the second equation above, because the poles from the first equations will only matter when seeking for correction terms of higher order than r^{-1} , which we will not pursue here. Recalling the last change of variables $w \rightarrow u$ we find that the poles are

$$u_{0\pm} = \pm \sqrt{2i\tilde{k}_0 r (1 - \sin \theta)} \equiv \pm \sqrt{2}\Lambda, \quad \Lambda = \sqrt{i\tilde{k}_0 r (1 - \sin \theta)}. \quad (\text{B13})$$

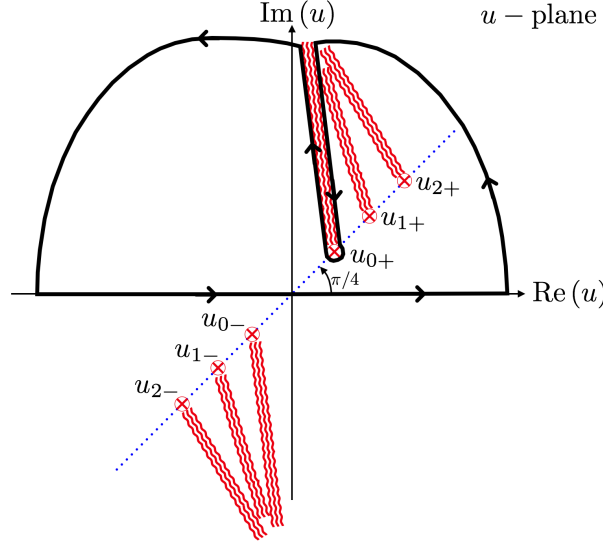


Figure 10: The path of integration C_u obtained by the conformal transformation given in Eq. (B10) when $\pi/2 > \theta \gg 0$. The path of steepest descent is mapped into the real axis of the u -plane. Here the branch points are

$$u_{0\pm} = u(\pi/2 - \theta) = \pm \sqrt{2i\tilde{k}_0 r (1 - \sin \theta)}, \quad u_{\pm 1} = u(-\pi/2 - \theta) = \pm \sqrt{2i\tilde{k}_0 r (1 + \sin \theta)} \quad \text{and} \\ u_{2\pm} = u(-\theta) = \pm \sqrt{2i\tilde{k}_0 r (1 - \cos \theta)}. \quad \text{The branch cuts converge at } \infty \times e^{i\pi/2} \text{ and } \infty \times e^{-i\pi/2}. \text{ When } \theta \approx 0 \text{ the} \\ \text{branch cuts lie over the blue dotted line of slope } \pi/4 \text{ and converge at the points } \infty \times e^{i\pi/4} \text{ and } \infty \times e^{i5\pi/4}.$$

Since our integration path is in the upper-half plane we require only u_{0+} .

From Eq. (B11) we realize that $F_1(u)$ is not a smooth function around the stationary phase $i\tilde{k}_0 z_0 \cos[\theta + \omega(u)]$ precisely due to the pole contribution, which prevents a direct application of the method. The main idea to overcome this difficulty is to subtract and add the conflicting pole as we will do next [1, 15]. This extraction procedure was mathematically justified by van der Waerden [57]. Due to the symmetry of the conformal transformation u in Eq. (B10) we will focus on the upper u -semi-plane. For this extraction, we need the residue of $F_1(u)$ at u_{0+} which is

$$\text{Res}(F_1; u_{0+}) = \frac{\sqrt{\tilde{k}_0 r}}{i\sqrt{i}}. \quad (\text{B14})$$

Then, we introduce the function

$$\psi(u) = \underbrace{F_1(u) - \frac{\text{Res}(F_1; u_{0+})}{u - u_{0+}}}_{\psi_1(u)} + \underbrace{\frac{\text{Res}(F_1; u_{0+})}{u - u_{0+}}}_{\psi_2(u)}. \quad (\text{B15})$$

In this way, $\psi_1(u)$ is analytic at u_{0+} , so that we can apply the standard steepest descent method. Meanwhile, $\psi_2(u)$ will contain the simple pole contribution that will be analyzed later. At this stage we rewrite \mathcal{H} in Eq. (B11) as

$$\mathcal{H}(\mathbf{x}, z_0; \omega) = \frac{\tilde{k}_0}{i} \sqrt{\frac{1}{2\pi \sin \theta}} \frac{e^{i\tilde{k}_0 r}}{r} [\mathcal{H}_{SD}(\mathbf{x}, z_0; \omega) + \mathcal{H}_P(\mathbf{x}, z_0; \omega)], \quad (\text{B16})$$

where we define

$$\mathcal{H}_{SD}(\mathbf{x}, z_0; \omega) = \oint_{C_u} du \psi_1(u) e^{-u^2/2}, \quad \mathcal{H}_P(\mathbf{x}, z_0; \omega) = \oint_{C_u} du \psi_2(u) e^{-u^2/2}. \quad (\text{B17})$$

The first contribution provides the standard steepest descent integral, and the second term results from the integration of the simple pole. For simplicity, we omit the explicit dependence of \mathcal{H}_{SD} and \mathcal{H}_P in what follows. For the moment, let us focus on \mathcal{H}_{SD} , whose detailed form is

$$\mathcal{H}_{SD} = \oint_{C_u} du \left\{ \frac{\sin^{5/2}[\theta + w(u)] e^{i\tilde{k}_0 z_0 \cos[\theta + w(u)]}}{\cos[\theta + w(u)]} - \frac{\sqrt{\tilde{k}_0 r}}{i\sqrt{i}(u - u_{0+})} \right\} e^{-u^2/2}. \quad (\text{B18})$$

As we mentioned previously, the u -transformation has already mapped the path of steepest descent into the real axis on the u -plane. Thus, we are able to approximate \mathcal{H}_{SD} with standard calculus techniques. Since we are interested only in the dominant term of \mathcal{H}_{SD} , it is enough to consider the zeroth order term in the expansion of $\psi_1(u)$ in its Taylor series around $u = 0$ ($w = 0$), because most of the contribution arises from its vicinity due to the presence of the gaussian function $e^{-u^2/2}$. Performing this, we obtain

$$\mathcal{H}_{SD} = \left\{ \frac{\sin^{5/2} \theta e^{i\tilde{k}_0 z_0 \cos \theta}}{\cos \theta} - \frac{1}{\sqrt{2(1 - \sin \theta)}} \right\} \sqrt{2\pi}, \quad (\text{B19})$$

where we have already introduced the expression of u_{0+} from Eq. (B13). Substituting back this result in Eq. (B16), we find

$$\mathcal{H} = \tilde{k}_0 \frac{e^{i\tilde{k}_0 r}}{ir} \left\{ \frac{\sin^2 \theta e^{i\tilde{k}_0 z_0 \cos \theta}}{\cos \theta} - \frac{1}{\sqrt{2(\sin \theta - \sin^2 \theta)}} \right\} + \frac{\tilde{k}_0}{i} \sqrt{\frac{1}{2\pi \sin \theta}} \frac{e^{i\tilde{k}_0 r}}{r} \mathcal{H}_P. \quad (\text{B20})$$

We observe that the first term inside the curly brackets is just the same term without the contribution of the simple pole that we reported in [44]. The second contribution appears to introduce divergences at $\theta = 0, \pi$, due to the term $1/\sqrt{\sin \theta}$. However, these singularities are artificial and arise from the insertion of the Hankel function $H_0^{(1)}$ in Eq. (B1) [15]. One can trace back these artificial divergences to the branch cuts represented by the ray that starts at the origin of Fig. 8a and Fig. 8b, by the ray that begins at $-\theta$ in Fig. 9b in the w -plane and by the ray that starts u_2 in Fig. 10 in the u -plane, after the successive transformations are performed. Nevertheless, we will prove later that these divergences are apparent as long as we work within the far-field approximation $\tilde{k}_0 r \rightarrow \infty$. It only remains to determine \mathcal{H}_P . As mentioned above, the u -transformation maps the path of steepest descent to the real axis on the u -plane. So, we only need to compute \mathcal{H}_P along that axis. Explicitly, we have that

$$\mathcal{H}_P = \frac{\pi \sqrt{\tilde{k}_0 r}}{\sqrt{i}} \frac{1}{i\pi} \int_{-\infty}^{\infty} du \frac{e^{-u^2/2}}{u - u_{0+}} \equiv \frac{\pi \sqrt{\tilde{k}_0 r}}{\sqrt{i}} \tilde{\mathcal{W}}(u_{0+}) = \frac{\sqrt{\pi \tilde{k}_0 r}}{i\sqrt{i}} Z(\Lambda), \quad (\text{B21})$$

recalling that $u_{0+} = \sqrt{2}\Lambda$ is given by Eq. (B13). We discuss some basic properties of the Faddeeva function $Z(\Lambda)$ and the function $\tilde{\mathcal{W}}$ in the Appendix C.

Substituting Eqs. (B21) and (C3) in Eq. (B20) yields our final expression for \mathcal{H}

$$\begin{aligned} \mathcal{H} = & \tilde{k}_0 \frac{e^{i\tilde{k}_0 r}}{ir} \left\{ \frac{\sin^2 \theta e^{i\tilde{k}_0 z_0 \cos \theta}}{\cos \theta} - \frac{1}{\sqrt{2(\sin \theta - \sin^2 \theta)}} \right\} \\ & + \sqrt{\frac{2}{\pi i \tilde{k}_0 r \sin \theta}} \frac{\tilde{k}_0^2}{i} e^{i\tilde{k}_0 r \sin \theta} \frac{\pi}{2} \operatorname{erfc} \left[-i \sqrt{i \tilde{k}_0 r (1 - \sin \theta)} \right], \end{aligned} \quad (\text{B22})$$

where the second term shows the presence of surface waves that arise directly from the simple pole contribution as Refs. [1, 15] establish. The expression for $\tilde{\mathcal{W}}$ is given in Eq. (C3).

Analogously, we obtain the form of \mathcal{H} in the LH, which indicates that the whole expression valid for both hemispheres is obtained by replacing $\cos \theta$ with $|\cos \theta|$ in Eq. (B22), yielding Eq. (24).

For the sake of completeness and consistency we show that Eq. (24) converges around $\theta = 0, \pi/2, \pi$. To deal with $\theta = \pi/2$ we find it convenient to set $\theta = \pi/2 - \xi$ in the UH and expand (24) in a power series of ξ around $\xi = 0$. We obtain

$$\mathcal{H}(\xi \rightarrow 0) \simeq \tilde{k}_0 \frac{e^{i\tilde{k}_0 r}}{ir} \left\{ i\tilde{k}_0 z_0 - \frac{\xi}{8} \right\} + \sqrt{\frac{2}{\pi i \tilde{k}_0 r}} \tilde{k}_0^2 e^{i\tilde{k}_0 r} \left(\frac{\pi}{2i} + \sqrt{\frac{\pi i \tilde{k}_0 r}{2}} \xi \right) + \mathcal{O}(\xi^2), \quad (\text{B23})$$

where we observe that the divergence disappeared. On the other hand, when $\theta \rightarrow 0$ we obtain

$$\begin{aligned} \mathcal{H}(\theta \rightarrow 0) &= -\tilde{k}_0 \frac{e^{i\tilde{k}_0 r}}{ir} \lim_{\theta \rightarrow 0} \frac{1}{\sqrt{2(\sin \theta - \sin^2 \theta)}} \\ &\quad + \lim_{\theta \rightarrow 0} \sqrt{\frac{\pi}{2i\tilde{k}_0 r \sin \theta}} \frac{\tilde{k}_0^2}{i} e^{i\tilde{k}_0 r \sin \theta} \left[-\frac{e^{i\tilde{k}_0 r(1-\sin \theta)}}{i\sqrt{i\pi\tilde{k}_0 r(1-\sin \theta)}} \right], \\ &= -\tilde{k}_0 \frac{e^{i\tilde{k}_0 r}}{ir} \lim_{\theta \rightarrow 0} \left[\frac{1}{\sqrt{2(\sin \theta - \sin^2 \theta)}} - \frac{1}{\sqrt{2(\sin \theta - \sin^2 \theta)}} \right] = 0, \end{aligned} \quad (\text{B24})$$

after using the asymptotic expansion of the function erfc [55], under the conditions $1 - \sin \theta \approx 1$ and $\tilde{k}_0 r \gg 1$ as required by the far-field approximation. Along the same lines we verify that $\mathcal{H}(\theta \rightarrow \pi)$ is also zero. The above discussion settles down the question posed after Eq. (B20), verifying the convergence of \mathcal{H} at $\theta = 0, \pi$. On the other hand, Eq. (B23) shows that the divergence located at $\theta = \pi/2$, whose origin is physical and emerges from the additional spherical symmetry breaking at the interface Σ between the two magnetoelectric media, has been already removed [40]. This could be understood in terms of the radiation that the observer receives. If the observer is far from the interface Σ (at angles $\theta = 0, \pi$ and large values of r), he will only receive spherical waves because the surface waves contribution decay rapidly far from the interface. Then, in that region there is no physical reason for a divergence in the electromagnetic field to occur, so that in the limits $\theta \rightarrow 0, \pi$, the integral \mathcal{H} must be well behaved as already proved in Eq. (B24). However, if the observer is near the interface Σ (at $\theta = \pi/2$ and large values of r), he will receive both spherical and surface waves because the maximal contribution of the latter is concentrated in the vicinity of Σ . The presence of surface waves reveals that the spherical symmetry is broken, which was manifest through the existence of the pole at $\theta = \pi/2$ (recall Eqs. (B11)-(B13) and Fig. 2), which now has been correctly removed as Eq. (B23) shows.

2. The integral \mathcal{J}

Now we proceed to determine the integral \mathcal{J} defined in Eq. (23). After introducing the Hankel function $H_0^{(1)}(k_\perp \rho)$ we write

$$\mathcal{J}(\mathbf{x}, z_0; \omega) = \frac{1}{2} \oint_{C_\perp} \frac{k_\perp dk_\perp}{\tilde{k}_0^2 - k_\perp^2} H_0^{(1)}(k_\perp \rho) e^{i\sqrt{\tilde{k}_0^2 - k_\perp^2}(|z| + z_0)}, \quad (\text{B25})$$

where C_{k_\perp} is the same path of integration shown in Fig. 8a. Once again we retain $1 \gg \text{Im}[\tilde{k}_0] > 0$. We observe that \mathcal{J} has almost the same form as (B2) except for the k_\perp^2 extra factor in the integrand. This will allow us to employ the previous results of the Appendix B1 exempting us from giving a detailed version of the calculations. After performing the same chain of transformations from the k_\perp -plane to the u -plane, which converted the integration path C_{k_\perp} of Fig. 8a into the path C_u of Fig. 10, we obtain

$$\mathcal{J}(\mathbf{x}, z_0; \omega) = \frac{e^{i\tilde{k}_0 r}}{i\tilde{k}_0 r} \sqrt{\frac{1}{2\pi \sin \theta}} \oint_{C_u} du F_2(u) e^{-u^2/2}, \quad F_2(u) = \frac{\sin^{1/2}[\theta + w(u)] e^{i\tilde{k}_0 z_0 \cos[\theta + w(u)]}}{\cos[\theta + w(u)] \sqrt{1 - \frac{u^2}{4i\tilde{k}_0 r}}}, \quad (\text{B26})$$

where again we restrict ourselves to the UH. Notice that $F_2(u)$ differs from $F_1(u)$ only in the exponent of the function $\sin[\theta + w(u)]$, which is a consequence of the distinct powers of k_\perp in the definitions of \mathcal{H} and \mathcal{J} . Since the singularities are the same, the separation of the pole yields

$$\zeta(u) = \underbrace{F_2(u) - \frac{\text{Res}(F_2; u_{0+})}{u - u_{0+}}}_{\zeta_1(u)} + \underbrace{\frac{\text{Res}(F_2; u_{0+})}{u - u_{0+}}}_{\zeta_2(u)}, \quad (\text{B27})$$

with u_{0+} given by Eq. (B13). Since $\zeta_1(u)$ is already analytic, we approximate its integral through the standard steepest descent method. Meanwhile, $\zeta_2(u)$ will contain the contribution of the simple pole. In this way, we rewrite \mathcal{J} as

$$\mathcal{J}(\mathbf{x}, z_0; \omega) = \frac{e^{i\tilde{k}_0 r}}{i\tilde{k}_0 r} \sqrt{\frac{1}{2\pi \sin \theta}} [\mathcal{J}_{SD}(\mathbf{x}, z_0; \omega) + \mathcal{J}_P(\mathbf{x}, z_0; \omega)], \quad (\text{B28})$$

where

$$\mathcal{J}_{SD}(\mathbf{x}, z_0; \omega) = \oint_{C_u} du \zeta_1(u) e^{-u^2/2}, \quad \mathcal{J}_P(\mathbf{x}, z_0; \omega) = \mathcal{H}_P(\mathbf{x}, z_0; \omega) = \oint_{C_u} du \zeta_2(u) e^{-u^2/2}. \quad (\text{B29})$$

The equality between \mathcal{J}_P and \mathcal{H}_P follows because $\text{Res}(F_2; u_{0+}) = \text{Res}(F_1; u_{0+})$. The remaining calculation of \mathcal{J}_{SD} follows the same steps as that of \mathcal{H}_{SD} (B18) in the Appendix B 1 and leads finally to Eq. (25), which can be shown to be convergent at $\theta = 0, \pi/2, \pi$.

The expansion of \mathcal{J} in the UH near the interface yields

$$\mathcal{J}(\xi \rightarrow 0) = \frac{e^{i\tilde{k}_0 r}}{i\tilde{k}_0 r} \left(i\tilde{k}_0 z_0 - \frac{\xi}{8} \right) + \sqrt{\frac{2}{\pi i\tilde{k}_0 r}} e^{i\tilde{k}_0 r} \left(\frac{\pi}{2i} + \sqrt{\frac{\pi i\tilde{k}_0 r}{2}} \xi \right) + O(\xi^2). \quad (\text{B30})$$

3. The integral \mathcal{I}

Now we move on to determine the integral \mathcal{I} defined in Eq. (22). After introducing the Hankel function $H_0^{(1)}(k_\perp \rho)$ and performing the chain of transformations from the k_\perp -plane to the u -plane previously described we obtain

$$\mathcal{I}(\mathbf{x}, z_0; \omega) = \frac{e^{i\tilde{k}_0 r}}{ir} \sqrt{\frac{1}{2\pi \sin \theta}} \oint_{C_u} du F_3(u) e^{-u^2/2}, \quad F_3(u) = \frac{\sin^{1/2}[\theta + w(u)] e^{i\tilde{k}_0 z_0 \cos[\theta + w(u)]}}{\sqrt{1 - \frac{u^2}{4i\tilde{k}_0 r}}}, \quad (\text{B31})$$

in the UH. Then, we realize that the only poles remaining in $F_3(u)$ are those arising from the square root in the denominator. Nevertheless we neglect them since, as previously mentioned in the Appendix B 1, these poles will only matter when we seek for correction terms of higher order than r^{-1} , which is not intended in this work. Therefore, this integral does not need a pole extraction in contrast with the former integrals \mathcal{H} and \mathcal{J} . Following the same steps previously carried on for \mathcal{H}_{SD} in the Appendix B 1 we obtain Eq. (26).

The expansion of \mathcal{I} in the UH near the interface is trivial and given by

$$\mathcal{I}(\xi \rightarrow 0) = \frac{e^{i\tilde{k}_0 r}}{ir} (1 + i\tilde{k}_0 z_0 \xi + O(\xi^2)). \quad (\text{B32})$$

Appendix C: Some properties of the function $Z(\Lambda)$

The function $Z(\Lambda)$ is known as the Faddeeva (plasma dispersion) function [1, 58] and has been much studied in the literature [16, 17, 59–61]. Let us recall the definition

$$Z(\Lambda) \equiv \frac{1}{\sqrt{\pi}} \int_{-\infty}^{+\infty} dx \frac{e^{-x^2}}{x - \Lambda} = i\sqrt{\pi} e^{-\Lambda^2} \text{erfc}(-i\Lambda), \quad (\text{C1})$$

where the last relation in Eq. (C1) in terms of the complementary error function

$$\text{erfc}(z) = 1 - \text{erf}(z) = \frac{2}{\sqrt{\pi}} \int_z^\infty dt e^{-t^2} \quad (\text{C2})$$

is taken from Refs. [1, 55], and yields

$$\tilde{W}(u_{0+}) = \frac{1}{i\sqrt{\pi}} Z(\Lambda) = i\pi e^{-i\tilde{k}_0 r(1-\sin \theta)} \text{erfc} \left[-i\sqrt{i\tilde{k}_0 r(1-\sin \theta)} \right]. \quad (\text{C3})$$

The function $\tilde{W}(u_0)$, already introduced in Eq. (B21), can be written in terms of the alternative expressions for the plasma dispersion function: $\omega(\Lambda)$ defined in Ref. [55] and $Z(\Lambda)$ defined in Ref. [58], as follows

$$\tilde{W}(u_{0+}) = \tilde{W}(\sqrt{2}\Lambda) = \omega(\Lambda) = \frac{1}{i\sqrt{\pi}} Z(\Lambda), \quad \Lambda = \sqrt{i\tilde{k}_0 r(1-\sin \theta)}, \quad (\text{C4})$$

where $\Lambda = x + iy$ is a complex variable, with x, y being real numbers.

The function $Z(\Lambda)$ satisfies the useful expression

$$Z(\Lambda^*) = -[Z(-\Lambda)]^*, \quad (\text{C5})$$

together with

$$Z(\Lambda) = i\pi^{1/2}e^{-\Lambda^2} - \Lambda \sum_{n=0}^{\infty} \pi^{1/2}(-\Lambda^2)^n/(n+1/2)!, \quad |\Lambda| \rightarrow 0, \quad (\text{C6})$$

$$Z(\Lambda) = i\pi^{1/2}\sigma(\Lambda)e^{-\Lambda^2} - \frac{1}{\Lambda} \sum_{n=0}^{\infty} \Lambda^{-2n}(n-1/2)!/\pi^{1/2}, \quad |\Lambda| \rightarrow \infty. \quad (\text{C7})$$

Here $\sigma(\Lambda) = 0, 1, 2$ when $y > 0$, $y = 0$, $y < 0$, respectively.

From Eq. (C4) we write $\Lambda = \sqrt{i}s = e^{i\pi/4}s$, $s = \sqrt{\tilde{k}_0 r (1 - \sin \theta)}$, and we require to calculate $Z(e^{i\pi/4}s)$ which we could read from Ref. [58]. However we find a misprint in the expression for $Z(e^{-i\pi/4}s)$ given there. The correct result is

$$Z(se^{-i\pi/4}) = i\pi^{1/2}e^{is^2} \left[1 + \sqrt{2}e^{-i3\pi/4} [C(t) - iS(t)] \right], \quad t = \sqrt{2/\pi}s, \quad (\text{C8})$$

where $C(t)$ and $S(t)$ are the Fresnel functions and with the identification $s = \rho$. From Eq. (C5) we obtain

$$Z(se^{i\pi/4}) = i\pi^{1/2}e^{-is^2} \left[1 + \sqrt{2}e^{i3\pi/4} [C(t) + iS(t)] \right], \quad (\text{C9})$$

which yields

$$|Z(se^{i\pi/4})|^2 = 2\pi \left[\frac{1}{2} + C^2(t) + S^2(t) - C(t) - S(t) \right]. \quad (\text{C10})$$

-
- [1] K. A. Michalski and J. R. Mosig, *The Sommerfeld half-space problem revisited: from radio frequencies and Zenneck waves to visible light and Fano modes*, Journal of Electromagnetic Waves and Applications, **30**:1, 1-42 (2016). <https://doi.org/10.1080/09205071.2015.1093964>
 - [2] T. I. Jeon and D. Grischkowsky, *THz Zenneck surface wave (THz surface plasmon) propagation on a metal sheet*, Appl. Phys. Lett. **88**, 061113 (2006). <https://doi.org/10.1063/1.2171488>
 - [3] L. Novotny, *Allowed and forbidden light in near-field optics. I. A single dipolar light source*, J. Opt. Soc. Am. A **14**, 91 (1997). <https://doi.org/10.1364/JOSAA.14.000091>
 - [4] S. A. Maier and H. A. Atwater, *Plasmonics: localization and guiding of electromagnetic energy in metal/dielectric structures*, Journal of Applied Physics **98**, 011101 (2005). <https://doi.org/10.1063/1.1951057>
 - [5] R. Gordon, *Surface plasmon nanophotonics: A tutorial*, IEEE Nanotechnology Magazine Vol. 2, No. 3, 12-18 (2008). <https://doi.org/10.1109/MNANO.2008.931481>
 - [6] A. Sommerfeld, *Über die Ausbreitung der Wellen in der drahtlosen Telegraphie*, Ann. Physik **28**, 665-736 (1909). <https://doi.org/10.1002/andp.19093330402>
 - [7] J. Zenneck, *Fortpflanzung ebener elektromagnetischer Wellen längs einer ebenen Leiterfläche*, Ann. Physik **23**, 846-866 (1907). <https://doi.org/10.1002/andp.19073281003>
 - [8] H. v. Hörschelmann, *Über die Wirkungsweise des geknickten Marconischen Senders in der drahtlosen Telegraphie*, Jb. drahtl. Telegr. u. Teleph. **5**, 14-34 and 188-211 (1911).
 - [9] A. Sommerfeld, *Über die Ausbreitung der Wellen in der drahtlosen Telegraphie*, Ann. Physik **81**, 1135-1153 (1926). <https://doi.org/10.1002/andp.19263862516>
 - [10] H. Weyl, *Ausbreitung elektromagnetischer Wellen über einem ebenen Leiter*, Ann. Physik **60**, 481-500 (1919). <https://doi.org/10.1002/andp.19193652104>
 - [11] M. J. O. Strutt, *Strahlung von Antennen unter dem Einfluss der Erdbodeneigenschaften*, Ann. Physik **1**, 721-772 (1929). <https://doi.org/10.1002/andp.19293930603>
 - [12] B. Van der Pol and K. F. Niessen, *Über die Ausbreitung elektromagnetischer Wellen über einer ebenen Erde*, Ann. Physik **6**, 273-294 (1930).
 - [13] G. S. Agarwal, *Quantum electrodynamics in the presence of dielectrics and conductors. I. Electromagnetic-field response functions and black-body fluctuations in finite geometries*, Phys. Rev. A **11**, 230 (1975). <https://doi.org/10.1103/PhysRevA.11.230>

- [14] A. Sommerfeld, *Partial Differential Equations in Physics*, New York: Academic Press, 1st ed., 1949 and 5th ed., 1967.
- [15] A. Baños *Dipole radiation in the presence of a conducting half-space*. New York, USA, Pergamon Press, 1966.
- [16] L. B. Felsen and N. Marcuvitz, *Radiation and Scattering of Waves*, Wiley-IEEE Press, 1973.
- [17] Brekhovskikh, L. M. *Waves in Layered Media*, Academic Press 2nd ed., New York, 1980.
- [18] See for example, P. C. Clemmow *The Plane Wave Spectrum Representation of Electro Magnetic Fields*, Pergamon Press, Oxford, 1966; G. Tyras, *Radiation and propagation of electromagnetic waves*, Academic Press, New York, 1969; K. C. Yeh and C. H. Liu, *Theory of ionospheric waves*, Academic Press, New York, 1972; J. A. Kong, *Theory of electromagnetic waves*, John Wiley & Sons Inc, 1975; J. R. Wait, *Electromagnetic Waves in Stratified Media*, Pergamon Press, 1962; J. R. Wait, *Wave Propagation Theory*, Pergamon, New York, 1981; J. R. Wait, *Electromagnetic wave theory*, Harper & Row, New York, 1985.
- [19] I. E. Dzyaloshinskii, *On the magneto-electrical effect in antiferromagnets*, JETP **10**, 628 (1960).
- [20] N. D. Astrof, *The magneto-electrical effect in antiferromagnets*, JETP **11**, 708 (1960).
- [21] M. Fiebig, *Revival of the magnetoelectric effect*, J. Phys. D: Appl. Phys. **38**, R123 (2005). <https://doi.org/10.1088/0022-3727/38/8/R01>
- [22] X. L. Qi, T. L. Hughes, S. C. Zhang, *Topological field theory of time-reversal invariant insulators*, Phys. Rev. B **78**, 195424 (2008). <https://doi.org/10.1103/PhysRevB.78.195424>
- [23] J. Wang, B. Lian, X. L. Qi, and S. C. Zhang, *Quantized topological magnetoelectric effect of the zero-plateau quantum anomalous Hall state*, Phys. Rev. B **92**, 081107(R) (2015). <https://doi.org/10.1103/PhysRevB.92.081107>
- [24] T. Morimoto, A. Furusaki, and N. Nagaosa, *Topological magnetoelectric effects in thin films of topological insulators*, Phys. Rev. B **92**, 085113 (2015). <https://doi.org/10.1103/PhysRevB.92.085113>
- [25] A. M. Essin, J. E. Moore, and D. Vanderbilt, *Magnetoelectric Polarizability and Axion Electrodynamics in Crystalline Insulators*, Phys. Rev. Lett. **102**, 146805 (2009). <https://doi.org/10.1103/PhysRevLett.102.146805>
- [26] M. Mogi, M. Kawamura, M. Kawamura, R. Yoshimi, A. Tsukazaki, Y. Kozuka, N. Shirakawa, K. S. Takahashi, M. Kawasaki, Y. Tokura, *A magnetic heterostructure of topological insulators as a candidate for an axion insulator*, Nat. Mater. **16**, 516-521 (2017). <https://doi.org/10.1038/nmat4855>
- [27] K. Nomura and N. Nagaosa, *Surface-Quantized Anomalous Hall Current and the Magnetoelectric Effect in Magnetically Disordered Topological Insulators*, Phys. Rev. Lett. **106**, 166802 (2011). <https://doi.org/10.1103/PhysRevLett.106.166802>
- [28] M. Z. Hasan, C. L. Kane, *Colloquium: Topological insulators*, Rev. Mod. Phys. **82**, 3045 (2010). <https://doi.org/10.1103/RevModPhys.82.3045>
- [29] X. L. Qi, S. C. Zhang, *Topological insulators and superconductors*, Rev. Mod. Phys. **83**, 1057 (2011). <https://doi.org/10.1103/RevModPhys.83.1057>
- [30] P. Sikivie, *Experimental Tests of the "Invisible" Axion*, Phys. Rev. Lett. **51**, 1415 (1983). <https://doi.org/10.1103/PhysRevLett.51.1415>
- [31] R. Peccei and H. Quinn, *CP Conservation in the Presence of Pseudoparticles*, Phys. Rev. Lett. **38**, 1440 (1977). <https://doi.org/10.1103/PhysRevLett.38.1440>
- [32] S. Weinberg, *The U(1) problem*, Phys. Rev. D **11**, 3583 (1975). <https://doi.org/10.1103/PhysRevD.11.3583>
- [33] F. Wilczek, *Two applications of axion electrodynamics*, Phys. Rev. Lett. **58**, 1799 (1987). <https://doi.org/10.1103/PhysRevLett.58.1799>
- [34] M. Kuster, G. Raffelt and B. Beltrán (eds), *Axions: Theory, Cosmology, and Experimental Searches* (Lecture Notes in Physics vol. 741) (Berlin: Springer-Verlag, 2008).
- [35] R. D. King-Smith and D. Vanderbilt, *Theory of polarization of crystalline solids*, Phys. Rev. B **47**, 1651(R) (1993). <https://doi.org/10.1103/PhysRevB.47.1651>
- [36] G. Ortiz and R.M. Martin, *Macroscopic polarization as a geometric quantum phase: Many-body formulation*, Phys. Rev. B **49**, 14202 (1994). <https://doi.org/10.1103/PhysRevB.49.14202>
- [37] J. D. Jackson. *Classical Electrodynamics* (Wiley, 3rd edition, New York, 1999).
- [38] A. Martín-Ruiz and L. F. Urrutia, *Interaction of a hydrogenlike ion with a planar topological insulator*, Phys. Rev. A **97**, 022502 (2018). <https://doi.org/10.1103/PhysRevA.97.022502>
- [39] W. Lukosz and R. E. Kunz, *Light emission by magnetic and electric dipoles close to a plane interface. I. Total radiated power*, J. Opt. Soc. Am. **67**, 1607-1615 (1977). <https://doi.org/10.1364/JOSA.67.001607>; W. Lukosz and R. E. Kunz, *Light emission by magnetic and electric dipoles close to a plane dielectric interface. II. Radiation patterns of perpendicular oriented dipoles*, J. Opt. Soc. Am. **67**, 1615-1619 (1977). <https://doi.org/10.1364/JOSA.67.001615>; M. A. Lieb, J. M. Zavislan, and L. Novotny, *Single-molecule orientations determined by direct emission pattern imaging*, J. Opt. Soc. Am. B **21**, 1210 (2004). <https://doi.org/10.1364/JOSAB.21.001210>
- [40] L. Novotny and B. Hecht. *Principles of Nano-optics*. Cambridge University Press, 2006.
- [41] J. Schwinger et al. *Classical Electrodynamics*. (Westview Press, Boulder, Colorado, 1998).
- [42] A. Martín-Ruiz, M. Cambiaso and L. F. Urrutia, *Green's function approach to Chern-Simons extended electrodynamics: An effective theory describing topological insulators*, Phys. Rev. D **92**, 125015 (2015). <https://doi.org/10.1103/PhysRevD.92.125015>; A. Martín-Ruiz, M. Cambiaso and L. F. Urrutia, *Electro- and magneto-statics of topological insulators as modeled by planar, spherical, and cylindrical θ boundaries: Green's function approach*, Phys. Rev. D **93**, 045022 (2016). <https://doi.org/10.1103/PhysRevD.93.045022>; A. Martín-Ruiz, M. Cambiaso and L. F. Urrutia, *Electromagnetic description of three-dimensional time-reversal invariant ponderable topological insulators*, Phys. Rev. D **94**, 085019 (2016). <https://doi.org/10.1103/PhysRevD.94.085019>
- [43] A. Martín-Ruiz, M. Cambiaso and L. F. Urrutia. *A Green's function approach to the Casimir effect on topological insulators with planar symmetry*, Europhysics Letters **113**, 60005 (2016). <https://doi.org/10.1209/0295-5075/113/60005>

- [44] O. J. Franca, L. F. Urrutia and Omar Rodríguez-Tzompantzi, *Reversed electromagnetic Vavilov-Čerenkov radiation in naturally existing magnetoelectric media*, Phys. Rev. D **99**, 116020 (2019). <https://doi.org/10.1103/PhysRevD.99.116020>
- [45] A. Sommerfeld, *Partial Differential Equations in Physics*, Academic Press, New York, 1964.
- [46] Chew, Weng Cho, *Waves and Fields in Inhomogenous Media*, IEEE Press Series on Electromagnetic Wave Theory. New York, 1990.
- [47] L. Mandel and E. Wolf, *Optical Coherence and Quantum Optics*. Cambridge University Press, 1995.
- [48] W. C. Chew, *A quick way to approximate a Sommerfeld-Weyl-type integral (antenna far-field radiation)*, IEEE Transactions on Antennas and Propagation Vol. 36, No. 11, 1654-1657 (1988). <https://doi.org/10.1109/8.9724>
- [49] J. R. Wait, *Electromagnetic waves in stratified media, Revised edition including supplemented material*, Pergamon Press, Oxford, 1970.
- [50] A. Crosse, S. Fuchs, S. Y. Buhmann, *Electromagnetic Green's function for layered topological insulators*, Phys. Rev. A **92**, 063831 (2015). <https://doi.org/10.1103/PhysRevA.92.063831>
- [51] L. Chen and S. Wan, *Critical surface band gap of repulsive Casimir interaction between three-dimensional topological insulators at finite temperature*, Phys. Rev. B **85**, 115102 (2012). <https://doi.org/10.1103/PhysRevB.85.115102>; W. Nie et al., *Casimir force between topological insulator slabs*, Phys. Rev. B **88**, 085421 (2013). <https://doi.org/10.1103/PhysRevB.88.085421>; R. Zeng et al., *Enhancing Casimir repulsion via topological insulator multilayers*, Phys. Lett. A **380**, 2861 (2016). <https://doi.org/10.1103/PhysRevB.88.085421>
- [52] S. S. Batsanov, E. D. Ruchkin, I. A. Poroshina, *Refractive Indices of Solids*, (SpringerBriefs in Applied Sciences and Technology, Singapore, 2016.
- [53] J. -P. Rivera, *A short review of the magnetoelectric effect and related experimental techniques on single phase (multi-) ferroics*, Eur. Phys. J. B **71**, 299 (2009). <https://doi.org/10.1140/epjb/e2009-00336-7>
- [54] X. L. Qi, R. D. Li, J. D. Zang, and S. C. Zhang, *Inducing a Magnetic Monopole with Topological Surface States*, Science **323**, 1184 (2009). <https://doi.org/10.1126/science.1167747>
- [55] M. Abramowitz and I. Stegun, *Handbook of Mathematical Functions with Formulas, Graphs and Mathematical Tables*, Dover Publications, New York, 1972.
- [56] G. Arfken and H. Weber. *Mathematical Methods for Physicists*. Elsevier Academic Press. 6a. ed. EUA, 2005.
- [57] B. L. Van der Waerden, *On the method of saddle points*, Appi. Sci. Res. **B 2**, No. 7, 33 (1950).
- [58] B. D. Fried and S. D. Conte, *The Plasma Dispersion Function: The Hilbert transform of the Gaussian*, New York, Academic Press, 1961.
- [59] A. Ishimaru, *Electromagnetic wave propagation, radiation and scattering*. Englewood Cliffs, New Jersey, Prentice Hall, 1991.
- [60] P. Baccarelli, P. Burghignoni, F. Frezza F, A. Galli, G. Lovat and D. R. Jackson, *Uniform analytical representation of the continuous spectrum excited by dipole sources in a multilayer dielectric structure through weighted cylindrical leaky waves*, IEEE Transactions on Antennas and Propagation, Vol. 52, No. 3, 653-665, 2004. <https://doi.org/10.1109/TAP.2004.825099>
- [61] R. E. Collin, *Hertzian dipole radiating over a lossy earth or sea: Some early and late 20th-century controversies*, IEEE Antennas and Propagation Magazine, Vol. 46, No. 2, 64-79, 2004. <https://doi.org/10.1109/MAP.2004.1305535>
- [62] T. Maruyama, et al., *Large voltage-induced magnetic anisotropy change in a few atomic layers of iron*, Nat. Nanotechnol. **4**, 158 (2009). <https://doi.org/10.1038/nnano.2008.406>
- [63] C. Bi, et al., *Reversible control of Co magnetism by voltage-induced oxidation*, Phys. Rev. Lett. **113**, 267202 (2014). <https://doi.org/10.1103/PhysRevLett.113.267202>
- [64] T. H. E. Lahtinen, K. J. A. Franke & S. van Dijken, *Electric-field control of magnetic domain wall motion and local magnetization reversal*, Sci. Rep. **2**, 258 (2012). <https://doi.org/10.1038/srep00258>